

ACTIVE MATTER

Collective clog control: Optimizing traffic flow in confined biological and robophysical excavation

J. Aguilar^{1*}, D. Monaenkova^{2*}, V. Linevich¹, W. Savoie², B. Dutta³, H.-S. Kuan⁴, M. D. Betterton⁵, M. A. D. Goodisman⁶, D. I. Goldman^{2†}

Groups of interacting active particles, insects, or humans can form clusters that hinder the goals of the collective; therefore, development of robust strategies for control of such clogs is essential, particularly in confined environments. Our biological and robophysical excavation experiments, supported by computational and theoretical models, reveal that digging performance can be robustly optimized within the constraints of narrow tunnels by individual idleness and retreating. Tools from the study of dense particulate ensembles elucidate how idleness reduces the frequency of flow-stopping clogs and how selective retreating reduces cluster dissolution time for the rare clusters that still occur. Our results point to strategies by which dense active matter and swarms can become task capable without sophisticated sensing, planning, and global control of the collective.

Diverse living (1) and artificial (2) active materials (3) and swarms spontaneously form clusters that can persist for long durations. However, for tasks that demand steady flow, such formations can be disadvantageous: Confined active systems such as pedestrian or vehicular traffic jams (4), competing bacterial biofilms (5), high-density migrating cells (6), jammed herds (7), and robot swarms (8) can produce high-density clogs that readily form glasslike arrests of flow (9). In such systems, the ability to dissolve clusters and prevent their formation (9), particularly in the absence of global knowledge of the state of all elements, is crucial.

Social insects (10) perform many tasks that demand clog minimization and mitigation. Substrate excavation specialists such as fire ants (*Solenopsis invicta*) cooperatively create nests of complex subterranean networks (Fig. 1A) consisting of tunnels in soil that support bidirectional traffic without lanes (11). Our previous laboratory experiments (12) revealed that, in the early stages of nest construction, the few-millimeter-long ants construct vertical tunnels approximately one body length in diameter (13). These narrow tunnels benefit the climbing ants as they transport bulky pellets, because close proximity to walls allows limbs, body parts, and antennae to aid slip recovery (12). But although

the structure of the tunnels seems to benefit individuals, physical-model experiments make it clear that excavation can suffer as a result of clogging during high-traffic conditions [e.g., (14) and Fig. 1C]. Here we use biological, theoretical, computational, and robophysical systems to show that counterintuitive behaviors—individual idleness and retreating—help optimize tunnel density by limiting the severity and prevalence of clogs, thereby enabling rapid excavation by the collective.

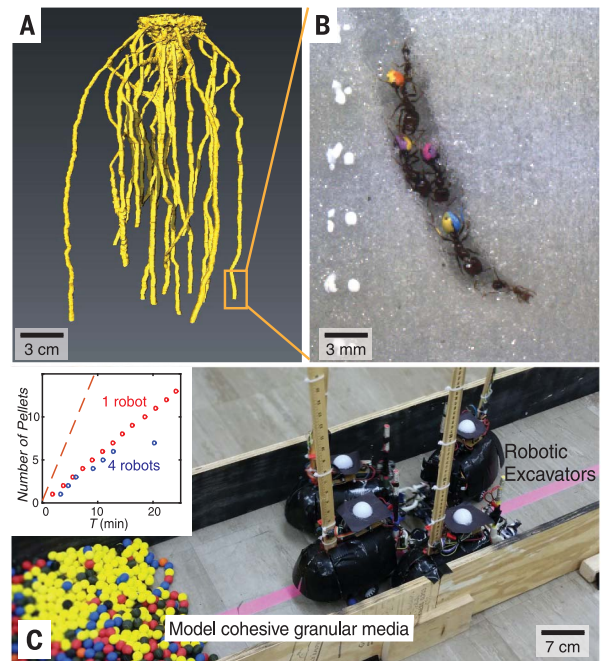
In laboratory experiments, we monitored the activity of fire ants as they excavated a cohesive

granular medium. Groups of ~30 workers were placed in transparent containers containing particle-water mixtures (13) consisting of 0.25-mm-diameter glass particles (Fig. 2A) with a soil moisture content, defined as the ratio of total water weight to total solid weight, of 0.01 or 0.1 (three trials each) (13). Ants excavated for 48 hours, with individual ants entering and exiting the tunnel hundreds of times. As in our previous study (12), ants constructed narrow vertical tunnels by means of a stereotyped process of grain and multigrain (pellet) removal and transport, followed by tunnel ascent and substrate deposition upon exit (13). A camera mounted to a motorized linear stage tracked a region within about three body lengths from the tunnel face (Fig. 2A and supplementary materials). We distinguished individual ant activity by marking ant abdomens with different colors (Fig. 1B). We recorded tunnel length over time (Fig. 2B), and the presence of each worker was logged when in the camera's view (Fig. 2C).

Ants exhibited a variety of behavioral tasks during collective excavation. A large fraction (0.22 ± 0.1 for soil moisture content of 0.01 and 0.31 ± 0.13 for soil moisture content of 0.1) of ants never entered the tunnel to excavate during the 48-hour period of observation; we refer to these as “nonvisitors.” As seen in Fig. 2C, ants that visited the tunnel face (“visiting” ants) varied in activity level. Inspired by work in honey bees (15), we quantified activity inequality among visitor ants using Lorenz curves. Points on the Lorenz curves in Fig. 2D link the cumulative fraction of workers in the population to the cumulative share of activity by that fraction. Although visitor ants' trips did not always result in the extraction of a pellet (see movie S1 and discussion

Fig. 1. Confined and crowded biological and robotic excavators.

(A) X-ray reconstruction of *S. invicta* fire ant excavation in a large container (25 cm wide) filled with 240- to 270- μ m-diameter glass particles (supplementary materials). (B) Painted *S. invicta* workers excavating a single tunnel along the wall of a transparent container with 0.25-mm-diameter wet glass particles. (C) Autonomous robotic diggers excavating in a simulated environment with cohesive granular media (diameter of 1.8 cm). The inset shows the number of pellets (defined as a cohesive group of grains) deposited versus time (7) by a robot excavating alone (red dots) and the net excavation of four robots (blue circles), whereby each robot attempts to excavate maximally. Orange dashed line indicates the hypothetical performance of the group of four robots in the absence of confinement.



¹School of Mechanical Engineering, Georgia Institute of Technology, Atlanta, GA 30332, USA. ²School of Physics, Georgia Institute of Technology, Atlanta, GA 30332, USA.

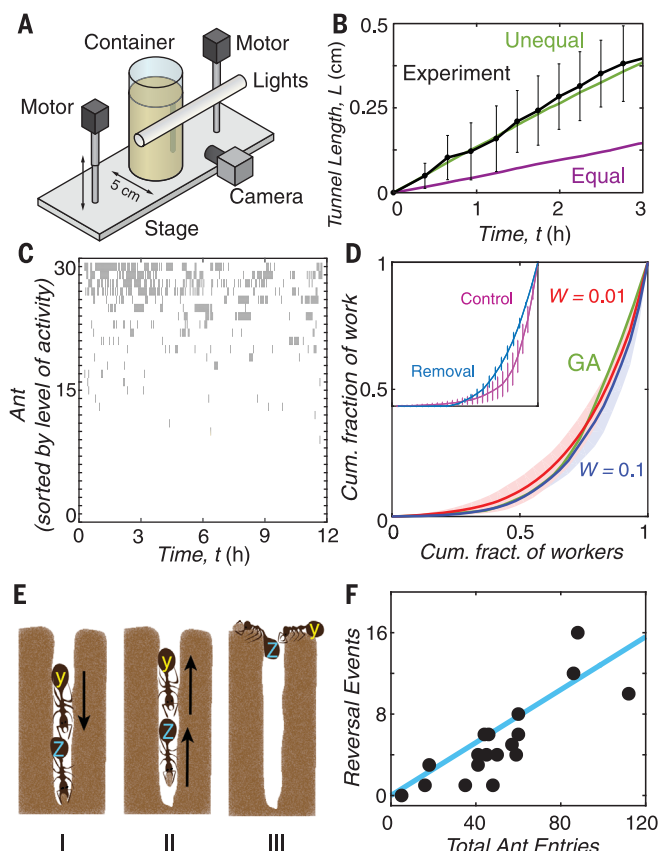
³School of Electrical and Computer Engineering, Georgia Institute of Technology, Atlanta, GA 30332, USA. ⁴Max Planck Institute for the Physics of Complex Systems, Nöthnitzer Str. 38, 01187 Dresden, Germany. ⁵Department of Physics, University of Colorado Boulder, Boulder, CO 80309, USA. ⁶School of Biological Sciences, Georgia Institute of Technology, Atlanta, GA 30332, USA.

*These authors contributed equally to this work.
†Corresponding author. Email: daniel.goldman@physics.gatech.edu

Fig. 2. Biological observations reveal workload inequality and reversal behaviors in ants.

(A) Experimental apparatus to track ant excavation; the inner diameter of the container is 5.21 cm. (B) The growth of tunnel length over time. Shown are average experimental results \pm SD/2 for *S. invicta* workers (black) and simulations for groups with equal (purple) and unequal (green) workload distribution. Error bars denote 1 SD in each direction. (C) “Visitation” map derived from experimental data. Each point in the map indicates the presence of a particular ant (out of 30 ants), ordered from most active (y axis) in the tunnel at a time t [soil moisture content (W) of 0.1]. (D) Lorenz curves for workload distributions obtained in wet

0.25-mm-diameter glass particles with soil moisture content of 0.1 (blue) and 0.01 (red) and a CA model (green) whose excavation rate was optimized with a GA. Shaded areas correspond to standard deviation from three experiments. cum., cumulative. The inset shows average Lorenz curves \pm SD/2 for a workload distribution within the group before (control, purple) and after (removal, blue) the most active diggers are removed from the group. Error bars correspond to standard deviations from three experiments. (E) Illustration of observed reversal behavior. (I) Ant Y’s path to excavate is blocked by ant Z. (II) After Z collects a pellet, it reverses, (III) forcing Y to reverse without excavating. (F) Total number of reversal events versus total ant visitors for the first 3 hours of ant excavation (soil moisture content of 0.1). Each data point represents total reversal events and total entries counted for 30-min segments collected from three experiments. Linear fit (blue line) with coefficient of determination (R^2) = 0.69.



below), we included these “reversals” in the Lorenz curve calculations because these animals expended energy in a trip to the tunnel face and contributed to tunnel traffic.

To characterize the Lorenz distributions, we calculated the Gini coefficient, G , defined as the ratio of the area between the Lorenz curve and the line of equality to the area under the line of equality (15). G is a measure of the deviation of the workload from perfectly shared ($G = 0$, all workers work equally) to completely unshared ($G = 1$, a single worker performs all work). Lorenz curves were characterized by $G = 0.75 \pm 0.10$ and displayed similar functional forms across a variety of experimental conditions (see Fig. 2D and fig. S2).

In the presence of competing tasks, like foraging or brood care, task allocation in ants can change depending on colony needs (16). To investigate temporal variation in ant excavation workload, we divided 48-hour experiments into

12-hour “epochs” (time periods). Although individual activity varied among epochs (Fig. 2C and fig. S3), the cumulative workload distribution was independent of epoch [one-way analysis of variance (ANOVA) $F_{3,20} = 0.85$, $P = 0.48$] and soil moisture content (one-way ANOVA, $F_{1,23} = 2.54$, $P = 0.13$) (Fig. 2D, figs. S1 and S2, and table S1). Furthermore, when the most active excavators were removed from the group, remaining workers increased their activity and compensated for the loss, preserving the shape of the Lorenz curve and therefore producing similar Gini coefficients (one-way ANOVA, $F_{1,4} = 1.13$, $P = 0.35$) (Fig. 2D, inset; table S2; and supplementary materials). Thus, given the consistency of the workload distribution, we hypothesize that variations in idleness (low activity levels) within a population may play an adaptive role in modulating the crowded conditions of confined tunnels and could have been important in the earliest social insect colonies (17).

Reversal behaviors were characterized by ants entering the tunnel and returning to the exit without carrying soil pellets. During the first 3 hours of the experiments, reversals occurred for $26 \pm 13\%$ of trips for soil moisture content of 0.01 and $18 \pm 3\%$ of trips for soil moisture content of 0.1. These events were often associated with local crowding at the excavation face (Fig. 2E) ($16 \pm 12\%$ of trips for soil moisture content of 0.01 and $10 \pm 2\%$ of observations for soil moisture content of 0.1). Reversal behaviors in crowded conditions occur on foraging trails (18), and similar phenomena have been observed in swarming bacteria (5). The incidence of this seemingly unproductive behavior increased with increasing overall activity of ants (Fig. 2F), suggesting that this behavior serves as a feedback mechanism for mitigating clogs during excavation.

To systematically examine the effects of idleness and individual retreating behaviors on excavation performance, we developed a cellular automata (CA) excavation model (Fig. 3A and supplementary materials). Such models are useful in elucidating the dynamics of biological and vehicular traffic (9, 19). The model consists of a lattice (the “tunnel”) with a width of two cells [similar to *S. invicta* tunnel widths (20)] occupied by soil, empty space, an ascending CA “ant,” and/or a descending CA ant (Fig. 3A). The CA ants can move, change directions, excavate, deposit a pellet, or rest. As in the biological experiments, activity for the workload distribution in the CA model was measured by counting instances when CA ants visited the tunnel within three body lengths (cells) of the excavation site.

We simulated the behavior of CA ants using both equal workload distributions (which we refer to as “active” CA ants) and unequal workload distributions (which we refer to as “Lorenz” CA ants) with identical reversal probabilities (movie S2). In unequal workload distributions, individual CA ants were assigned individual “entrance probabilities” defined as the probability that a CA ant will enter the tunnel. The initial entrance probability distribution for the 30 CA ants was taken from the biological distribution. Output workload distributions of CA simulations closely matched the input entrance probability distributions (as measured by the Gini coefficient, fig. S25). During a time-step, if its path toward the excavation area was blocked, a CA ant would reverse direction toward the exit with a probability, R , of 0.34 (supplementary materials); R was set by the proportion of total reversal events observed for 0.01 soil moisture in the biological experiments.

The CA model that used unequal workload distribution and reversals reproduced experimentally observed biological ant digging rates (Fig. 2B). To determine if these rates represented an optimal workload distribution, we used a genetic algorithm (GA) (fig. S24) to select for entrance probability distributions (supplementary materials) that maximized excavated tunnel length within a given duration. Regardless of the initial population distribution (either similar to the ants or highly unequal), within a

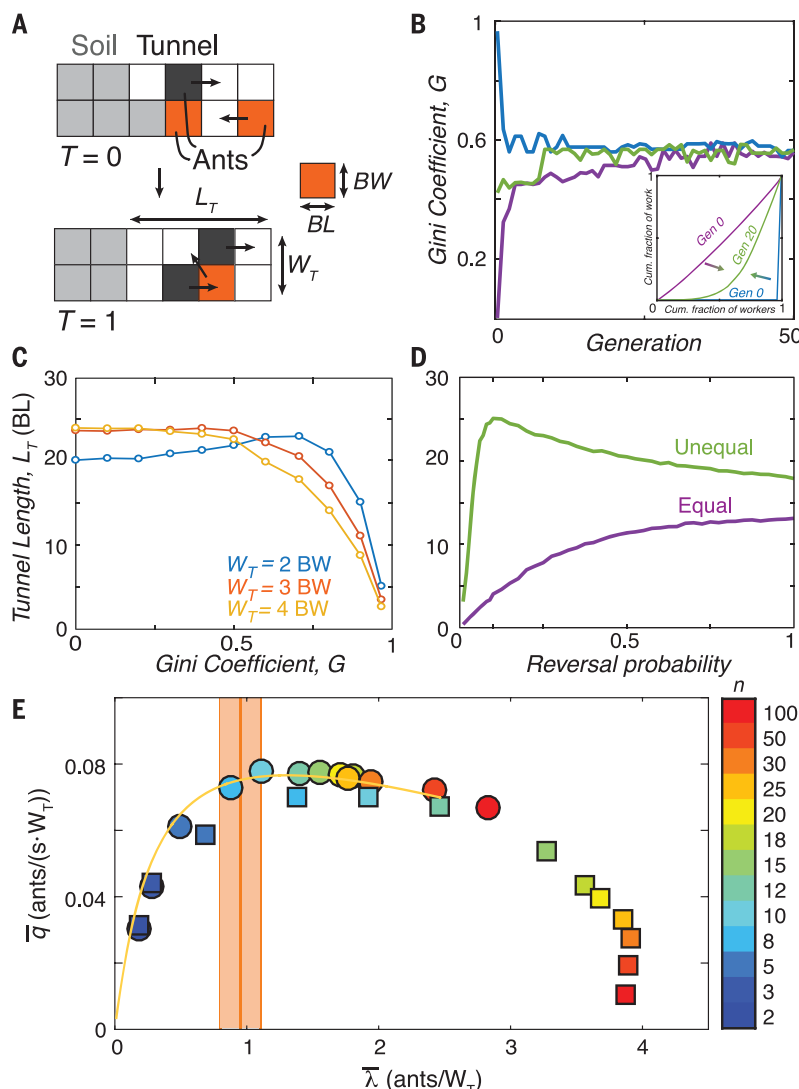


Fig. 3. Models reveal optimized traffic flow in narrow tunnels by means of selective retreating and workload inequality. (A) Schematic showing the main components of the CA model. Cell colors denote soil (light gray), tunnel (white), ants moving toward the excavation site (orange), and ants exiting the tunnel (dark gray). T , simulation time-step. (B) Gini coefficient over time under GA optimization for groups started with a completely equal (purple), completely unequal (blue), and random (green) workload distribution. Lorenz curves (inset) for groups that begin with complete equality or inequality rapidly reach a similar workload distribution. (C) Excavated tunnel length, L_T , after 24-hour simulation time versus Gini coefficient for tunnels of different widths, W_T , for a 30-CA ant population. BL, body length; BW, body width. (D) Excavated tunnel length after 24-hour simulation time versus reversal probability for equal and unequal (optimized for 30 CA ants) workload distributions. (E) Simulated traffic flow (\bar{q} , number of ants divided by time in seconds times tunnel width) versus CA ant occupancy ($\bar{\lambda}$, number of ants divided by tunnel width, measured in excavator body widths) for groups of equally (squares) and unequally (circles) active ants. Color bar indicates the size, n , of the excavating group. The theoretical fundamental diagram of the OAT model (yellow curve) illustrates the need to limit tunnel traffic to one worker per body width of tunnel width to optimize flow and prevent deleterious clogs. Experimental ant observations reveal an average occurrence around this density (orange-shaded region, where the orange centerline is the mean and the extents are one standard deviation away from the mean).

few generations, the GA simulation converged to an unequal workload distribution (Fig. 3B, for a 30-ant example), which was similar to the experimentally observed biological workload distributions (Fig. 2D, green).

The CA model also revealed the importance of the reversal behavior in conjunction with unequal workload distributions. Although the active excavation could be improved by sufficient reversal probability, only a small amount of reversal was

needed to increase the excavation performance in the unequal distribution (Fig. 3D). Thus, in addition to the benefits narrow tunnels provide for climbing and pellet transport (12, 13), we hypothesize that the ants benefit from narrow tunnels by expending less energy to dig wider tunnels to the same depth. Such benefits would be useful in the early stages of new nest construction (e.g., after the colony is flooded out) during which establishing the colony underground is critical.

To gain insight into other benefits and constraints set by such narrow tunnels, we simulated 30 CA ants with varied workload distributions (characterized by distinct Gini coefficients) in tunnels of different widths. These distributions were created through a randomized Monte Carlo process, such that the Lorenz curves resulted in desired Gini coefficients. A peak in excavated length, L , versus Gini coefficient was observed in a tunnel two cells wide (Fig. 3C). Wider tunnels (three and four cells wide) resulted in broader performance peaks, indicating a decreased sensitivity in performance owing to workload distribution. This indicates that use of a narrow tunnel necessitates the “discovery” of the unequal workload distribution of ants.

We hypothesized that the unequal workload distribution and reversals were linked to uniform flow of CA ants in the tunnel. We therefore measured the average flow rate of successful excavators, \bar{q} , versus the average tunnel-width-normalized occupancy of excavators, $\bar{\lambda}$ (the ratio of average number of ants in the tunnel to tunnel width measured in ant body widths). To generate a wide range of average occupancies, we varied the population size of the CA system.

The flow rate was optimal at an intermediate occupancy (Fig. 3E). This nonmonotonic trend in \bar{q} versus $\bar{\lambda}$ is characteristic of various multi-agent systems, including bridge-building army ants (21) and vehicle traffic (22, 23), and is referred to in traffic literature as the “fundamental diagram” (24). Active ants, which do not modulate their workload distribution, increase tunnel occupancy with increasing population and thus exhibit optimal flow rates for only a few population sizes. By contrast, GA-optimized Lorenz ants produced tunnel occupancies in the ideal range by generating increasingly unequal workload distributions for increasing CA ant population sizes. Of particular importance, fire ants produced tunnel densities in the ideal range (Fig. 3E, orange-shaded region).

The ability of the ants to operate at the optimum in the fundamental diagram and the rapidity by which the GA model converges (Fig. 3B) indicate the existence of a simple governing principle for traffic control in confined task-oriented systems. To elucidate this principle, we formulated a minimal model of ant traffic in the narrowest (single-lane) tunnel: the one-at-a-time (OAT) model. This model, which builds on recent work on traffic of motor proteins on microtubules (25), allows us to estimate analytically how the excavation rate varies with the rate of ants entering the tunnel (supplementary materials) for various work-distribution strategies.

In the OAT model, ants enter the tunnel and move toward its face; descending ants reverse direction if they either reach the end of the tunnel or collide with an ant moving in the other direction (supplementary materials). We initially modulated occupancy by varying the entrance probability of all ants equally; as in the CA model, the flow rate of the OAT model was optimal at an intermediate width-normalized ant occupancy (Fig. 3E, yellow curve, and supplementary materials)—in particular, one excavator for every excavator that can fit along the width of the tunnel. Although the peak in the fundamental diagram has been associated with the transition between steady flow and propagating traffic jams (24), the OAT model highlights a key feature of confined tunnel excavation: Traffic dynamics are driven by tunnel width. Given the task-oriented nature of the system, successful traffic flow is only possible if a worker can travel the entire length of the tunnel and back. Thus, if there are enough workers in the tunnel to clog the path to or from the excavation site, traffic is likely to slow down. The OAT model highlights this scenario, as such clogs are unavoidable if more than one ant is in the single-lane tunnel. Because ants cannot pass each other or change lanes, only the first ant to enter can reach the end to excavate, whereas other workers collide with the first worker, reverse, and impede traffic.

Mechanisms that target a specific number of excavators occupying the tunnel given the tunnel's width promote ideal traffic flow. When individual ants in the OAT model were programmed to modulate their rate of reentry according to how often they reversed without excavating, the OAT model rapidly converged to Lorenz curves similar to the biological and GA-optimized CA ants (supplementary materials and fig. S23). Such rapid convergence highlights the benefit of targeting a specific number of ants (in this case, by establishing unequal workload distributions) in narrow tunnels.

We next used a system of excavating robots (fig. S9) to test if the above theoretical strategies could improve traffic in confined experimental situations with more complex, unpredictable interactions. Because, presently, robot mobility in real-world environments is poor relative to biological systems and because real collisional interactions not modeled in CA and OAT are typically neglected in swarming robot studies (2), such robophysical (26) studies can aid robot design and control for real-world robot swarms, as well as suggest hypotheses for studies of ant traffic (18), adaptive behaviors, and morphological features for crowded excavation and movement.

Groups of roughly elliptical robots (movie S3) with similar aspect ratios to the biological ants were tasked with excavating a model cohesive granular medium of hollow plastic spheres containing loose magnets; this design allows clumps of media to be formed, analogous to the pellets of cohesive soil formed by the biological ants (13). Our robots followed simple instructions

triggered by onboard sensory feedback of the surrounding environment (supplementary materials). Previous work in swarm robotics (27) used similar decentralized strategies in conjunction with collision-avoidance schemes (2, 28) to produce emergent flocking behavior. By con-

trast, our robots detected collisions with push switches on their outer shell, which triggered navigation strategies such as steering away and readjusting to promote clog resolution (movie S4).

To challenge the robots, we constructed a tunnel (Fig. 4A) with a width of three robot

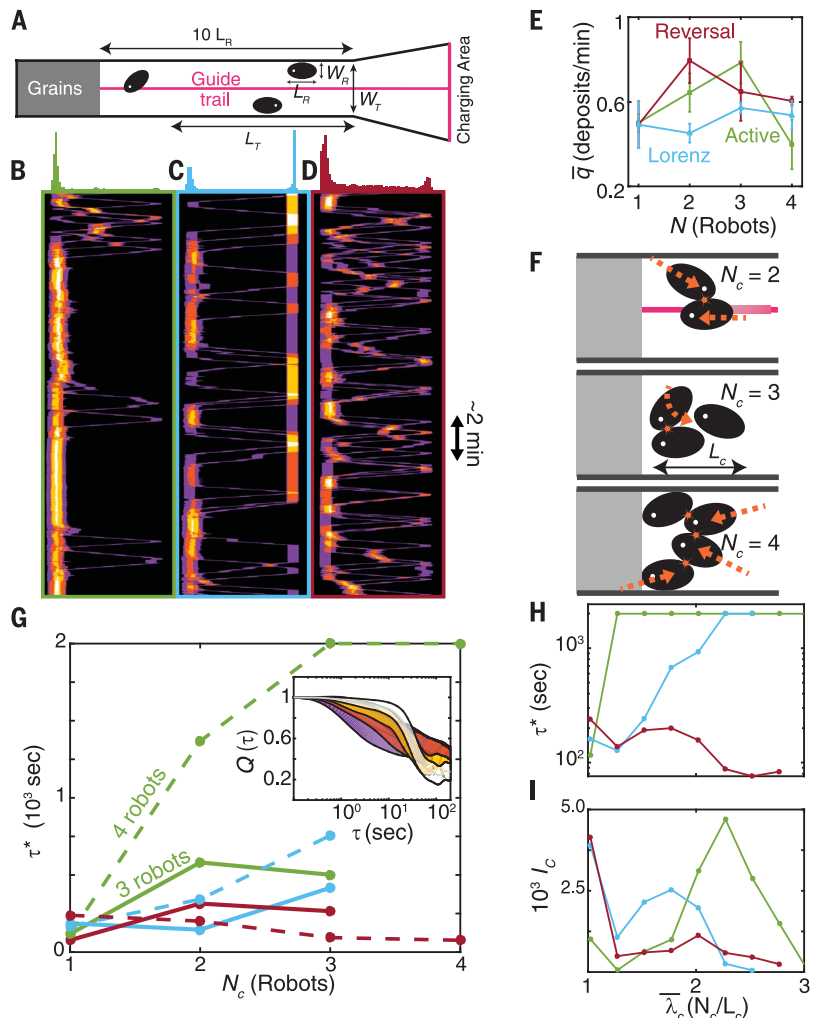


Fig. 4. Traffic flow and local dynamics during robot excavation. (A) Schematic of the excavation arena indicating the tunnel length, L_T (excluding the excavation area); robot width, W_R ; robot length, L_R ; and tunnel width, W_T . A pink centerline along the tunnel was monitored by the robots' onboard cameras, enabling them to follow the tunnel path. (B to D) Experimental space-time overlap heat maps of robot positions (x axis) for four-robot trials of (B) active digging, (C) Lorenz digging, and (D) reversal digging. Color indicates the number of robots occupying a particular space and time: one (purple), two (orange), three (yellow), and four (white) robots. Histograms above the graphs show the frequency of occurrence of clusters with two or more robots at different lateral positions. (E) Average flow rate, \bar{q} , \pm SD measured in deposits per minute versus number of robots in the experiment, N , for active (green), Lorenz (light blue), and reversal (maroon) strategies. (F) Illustration of various collision scenarios encountered by robots owing to movement toward guide trail (top), turning (middle), and forward-backward translation (bottom). Orange starbursts indicate collisions. (G to I) Relaxation times for all strategies: active (green), Lorenz (light blue), and reversal (maroon). (G) Relaxation time versus cluster size, N_c , for three-robot (solid) and four-robot (dashed) trials. The inset shows sample average correlation curves, $Q(\tau)$, that measure how $N_c = 1$ (purple), 2 (orange), 3 (yellow), and 4 (white) robot clusters dissolve over time during four-robot reversal trials; shaded region indicates average curves \pm SD/2 (standard deviations for τ^* range from 100 to 500 s). (H) Relaxation times versus linear aggregation density, $\bar{\lambda}_c$, for four-robot trials and (I) corresponding number of cluster occurrences, I_c , versus linear aggregation density.

widths (or 1.5 robot lengths), which, combined with the oblong robot shape, forced a challenge of turning around in confined spaces. We tracked the positions (supplementary materials and fig. S10) of the robots in the main tunnel area (i.e., excluding the excavation site) to generate space-time overlap maps of robot positions (see Fig. 4, B to D), which give visual insight into robot flow during excavation.

We first examined systematically how excavation performance changed as numbers of robots increased for our active protocol (as in Fig. 1C and fig. S6), which assigned equal work “desire” to all diggers: After soil deposition, each robot immediately returned to the tunnel to excavate. Despite constraints on maneuverability, sensing, and morphology, the robophysical experiments demonstrated qualitatively similar performance to the ants and the computational and theoretical models. For example, measurement of the average flow rate, \bar{q} , of successful excavators (which we quantify here as the number of deposits per minute) revealed that excavation performance increased with an increasing number of robots in the trial (N) until the system became sufficiently crowded (Fig. 4E).

To characterize how clustering led to performance degradation in the active protocol, we measured the frequency of cluster occurrences, denoted I_c . Here we defined clusters as groups of robots of number N_c , whose center positions were within a robot length of each other (supplementary materials). Such clusters occurred most frequently at the excavation site (histograms in Fig. 4, B to D), yielding phase separation (29) in the system, whereby a portion of robots were jammed at high density, whereas others moved smoothly through the tunnel at low density.

As in (9), we also measured the characteristic “relaxation” times for clusters using a tool from the study of glassy systems, the density overlap correlation function $Q(\tau)$. $Q(\tau)$ compares the spatial overlap of a cluster at a specific time to the overlap of the cluster’s original lateral segment at a later time, τ . Assuming a one-dimensional tunnel, we calculated the spatial overlap of robots by tracking their centroid position laterally (along the tunnel) and assigning intensity potentials in space, summing overlapping potentials of adjacent robots (fig. S12A). From these curves (Fig. 4G, inset; fig. S12; and supplementary materials), we calculated the relaxation time, τ^* , for clusters of different N_c by fitting a stretched exponential function, $Q_f(\tau) = \exp\left\{-\left(\frac{\tau}{\tau^*}\right)^\beta\right\}$, to a Q curve averaged over clusters of the same N_c , where β is a fitting parameter that is of order unity.

The relaxation time analysis highlighted how sufficient numbers of active robots ($N = 4$) resulted in clustering cascades. For example, $N_c = 2$ robot clusters could be sufficiently difficult to resolve before a third robot joined the cluster, which in turn led to catastrophic $N_c = 4$ robot jams that spanned the tunnel width. Such clogs were then difficult to resolve with the

robots’ limited sensory and motor capabilities and were likely exacerbated by the robots’ rigid oblong shape (Fig. 4F). A sharp increase in τ^* for clusters with a linear density, $\bar{\lambda}_c = N_c/L_c$, where L_c is cluster length in body lengths, greater than unity (multirobot clusters) during four-robot active trials (Fig. 4H, green curve) revealed how this cascading scenario is reminiscent of glassy arrest in particulate systems (30, 31).

To discover how the strategies of idleness distributions and reversals affected clustering and traffic dynamics in the robots (movie S5), we implemented two protocols inspired by the biological observations and theoretical models. As in the CA model, in the Lorenz protocol (fig. S8), we implemented an unequal probability to enter the tunnel derived from experimental ant workload inequalities. We also implemented a separate robot reversal protocol (fig. S7), which produced selective retreats, whereby the robots were programmed to immediately resume excavation after deposition but reversed after not successfully reaching the excavation site within a given time. These strategies led to different excavation performances as N increased; but most importantly, both strategies outperformed the active protocol at $N = 4$ (Fig. 4E).

The relaxation times and cluster analysis revealed the mechanisms by which the different protocols mitigated clogging, particularly in the distinct ways in which they reduced the duration of clusters and thus optimized the average occupancy of excavators, thereby improving traffic flow. For trials with up to three robots, all strategies produced a relatively low τ^* (Fig. 4G) and frequency of cluster occurrence regardless of the number of robots in a cluster. However, for $N = 4$, the Lorenz and reversal protocols mitigated the clogging effects associated with the aggressive excavation in the active protocol.

The Lorenz and reversal protocols provided distinct forms of mitigating the catastrophic cascades of clogs found in the active protocol: Unequal workload distributions reduce the occurrence of clusters, and selective retreating limits the duration of clogs. Selective retreating in the reversal strategy limited the duration of clogs. Thus, instead of the glass-forming characteristics of active robots, clusters dissolved after some time, yielding low τ^* (Fig. 4, G and H). The unequal workload distributions of the Lorenz strategy reduced the occurrence of clusters, especially the highest-density four-robot clusters (Fig. 4I), where glasslike clog formation is most likely to occur, resulting in fewer catastrophic clogs at the excavation site. We found similar evidence for clog mitigation in the analysis of clusters in the CA model (fig. S26 and supplementary materials), whereby clog mitigation was further found to be most effective when both strategies (reversals and unequal entrance probabilities) were used in combination.

To close, we return to the traffic aspects of the confined system: As in theory, traffic flow of robotic ants (which dominates the excavation performance) was maximal at an intermediate occupancy of excavators, $\bar{\lambda} = N_T/W_T$, where N_T is

the number of robots in the main tunnel area averaged across all frames of video and W_T is the width of the tunnel, followed by a gradual decline at higher $\bar{\lambda}$ (fig. S11A). However, unlike the theoretical models, peak flow rate in robotic systems occurred at a $\bar{\lambda}$ of approximately 0.25, which corresponds to less than one robot traversing the tunnel at a time, despite a tunnel width of about three robot widths, or 1.5 robot lengths.

We hypothesize that the underperformance of our robots relative to the biological and theoretical systems is a consequence of our robots’ limited mobility in confined spaces, indicating that deformable bodies (32) and novel locomotor mechanisms (12) will be important in confined real-world robot collectives. That said, given these strategies are robust to the vagaries of real-world interactions, we posit that other engineered systems—including robot swarms in disaster rubble, nanorobots surging through the bloodstream (33), and task-capable active materials (3)—could benefit from simple strategies that involve labor inequality, particularly in creative combinations (34).

REFERENCES AND NOTES

1. A. Okubo, *Adv. Biophys.* **22**, 1–94 (1986).
2. M. Brambilla, E. Ferrante, M. Birattari, M. Dorigo, *Swarm Intell.* **7**, 1–41 (2013).
3. M. Marchetti et al., *Rev. Mod. Phys.* **85**, 1143–1189 (2013).
4. D. Helbing, *Rev. Mod. Phys.* **73**, 1067–1141 (2001).
5. N. C. Dantton, L. Turner, S. Rojevsky, H. C. Berg, *Biophys. J.* **98**, 2082–2090 (2010).
6. E. Méhes, T. Vicsek, *Integr. Biol. (Camb.)* **6**, 831–854 (2014).
7. A. Garcimartín et al., *Phys. Rev. E Stat. Nonlin. Soft Matter Phys.* **91**, 022808 (2015).
8. L. Giomi, N. Hawley-Weld, L. Mahadevan, *Proc. R. Soc. London A Math. Phys. Sci.* **469**, 20120637 (2013).
9. N. Gravish, G. Gold, A. Zangwill, M. A. D. Goodisman, D. I. Goldman, *Soft Matter* **11**, 6552–6561 (2015).
10. D. M. Gordon, *Nature* **380**, 121–124 (1996).
11. D. Cassill, W. R. Tschinkel, S. B. Vinson, *Insectes Soc.* **49**, 158–163 (2002).
12. N. Gravish, D. Monastanova, M. A. Goodisman, D. I. Goldman, *Proc. Natl. Acad. Sci. U.S.A.* **110**, 9746–9751 (2013).
13. D. Monastanova et al., *J. Exp. Biol.* **218**, 1295–1305 (2015).
14. V. Linevich, D. Monastanova, D. I. Goldman, *Artif. Life Robot.* **21**, 460–465 (2016).
15. P. Tenczar, C. C. Lutz, V. D. Rao, N. Goldenfeld, G. E. Robinson, *Anim. Behav.* **95**, 41–48 (2014).
16. E. J. Robinson, O. Feinerman, N. R. Franks, *Proc. Biol. Sci.* **276**, 4373–4380 (2009).
17. D. M. Gordon, *Cell Syst.* **3**, 514–520 (2016).
18. V. Fourcassié, A. Dussutour, J. L. Deneubourg, *J. Exp. Biol.* **213**, 2357–2363 (2010).
19. A. John, A. Schadschneider, D. Chowdhury, K. Nishinari, *J. Theor. Biol.* **231**, 279–285 (2004).
20. N. Gravish et al., *J. R. Soc. Interface* **9**, 3312–3322 (2012).
21. C. R. Reid et al., *Proc. Natl. Acad. Sci. U.S.A.* **112**, 15113–15118 (2015).
22. C. Gershenson, D. Helbing, *Complexity* **21**, 9–15 (2015).
23. K. Nagel, M. Schreckenberg, *J. Phys. I* **2**, 2221–2229 (1992).
24. R. Kühne, in *Highway Capacity and Level of Service: Proceedings of the International Symposium on Highway Capacity*, Karlsruhe, 24–27 July 1991, U. Brannolte, Ed. (CRC Press, 1991).
25. H.-S. Kuan, M. D. Betterton, *Phys. Rev. E* **94**, 022419 (2016).
26. J. Aguilar et al., *Rep. Prog. Phys.* **79**, 110001 (2016).
27. M. J. Mataric, in *From Animals to Animals 2: Proceedings of the Second International Conference on Simulation of Adaptive Behavior*, J.-A. Meyer, H. L. Roitblat, S. W. Wilson, Eds. (MIT Press, 1993), pp. 432–441.
28. U. Borrmann, L. Wang, A. D. Ames, M. Egerstedt, *IFAC-PapersOnLine* **48**, 68–73 (2015).
29. G. S. Redner, M. F. Hagan, A. Baskaran, *Phys. Rev. Lett.* **110**, 055701 (2013).

30. D. I. Goldman, H. L. Swinney, *Phys. Rev. Lett.* **96**, 145702 (2006).
31. H.-S. Kuan, R. Blackwell, L. E. Hough, M. A. Glaser, M. D. Betterton, *Phys. Rev. E Stat. Nonlin. Soft Matter Phys.* **92**, 060501 (2015).
32. K. Jayaram, R. J. Full, *Proc. Natl. Acad. Sci. U.S.A.* **113**, E950–E957 (2016).
33. S. Li *et al.*, *Nat. Biotechnol.* **36**, 258–264 (2018).
34. W. Liu, A. F. Winfield, J. Sa, J. Chen, L. Dou, *Adapt. Behav.* **15**, 289–305 (2007).

ACKNOWLEDGMENTS

The authors thank W. Gardner, Griffin Botanical Garden, and Chattahoochee-Oconee National Forest for giving us permission for ant collection. We would also like to acknowledge N. Gravish for insight and fruitful discussions; M. Kingsbury and L. Chen for

assistance in magnetic particle construction; R. Kutner, R. Srivastava, and J. Logan for their help with video analysis; and N. Conn for help with ant collection. H.-S.K. thanks the Max Planck Institute for the Physics of Complex Systems for providing computing resources. **Funding:** The authors acknowledge the support of National Science Foundation grants NSF PoLS-0957659, PHY-1205878, and DMR-1551095, as well as ARO grant W911NF-13-1-0347, the National Academies Keck Futures Initiative, and the Dunn Family Professorship (to D.I.G.). **Author contributions:** B.D. and D.M. collected the raw data for the ant experiments. W.S. and D.M. developed and performed the CA simulations. H.-S.K. and M.D.B. developed and analyzed the OAT model. V.L. constructed and performed the ant robot experiments, and J.A. tracked and analyzed the robot experiment data. All authors contributed to the preparation of the manuscript and were involved in the interpretation of results. **Competing interests:** The

authors declare that they have no competing interests. **Data and materials availability:** Data are available on SMARTech at <https://smartech.gatech.edu/>.

SUPPLEMENTARY MATERIALS

www.sciencemag.org/content/361/6403/672/suppl/DC1
Materials and Methods
Figs. S1 to S26
Tables S1 to S4
References (35–41)
Movies S1 to S5

6 April 2017; resubmitted 17 January 2018
Accepted 14 June 2018
10.1126/science.aan3891

Collective clog control: Optimizing traffic flow in confined biological and robophysical excavation

J. Aguilar, D. Monaenkova, V. Linevich, W. Savoie, B. Dutta, H.-S. Kuan, M. D. Betterton, M. A. D. Goodisman and D. I. Goldman

Science **361** (6403), 672-677.
DOI: 10.1126/science.aan3891

When fewer workers are more efficient

A narrow passageway can easily become clogged or jammed if too much traffic tries to enter at once or there is competition between the flow of traffic in each direction. Aguilar *et al.* studied the collective excavation observed when ants build their nests. Because of the unequal workload distribution, the optimal excavation rate is achieved when a part of the ant collective is inactive. Numerical simulations and the behavior of robotic ants mimic the behavior of the colony.

Science, this issue p. 672

ARTICLE TOOLS

<http://science.sciencemag.org/content/361/6403/672>

SUPPLEMENTARY MATERIALS

<http://science.sciencemag.org/content/suppl/2018/08/15/361.6403.672.DC1>

REFERENCES

This article cites 36 articles, 8 of which you can access for free
<http://science.sciencemag.org/content/361/6403/672#BIBL>

PERMISSIONS

<http://www.sciencemag.org/help/reprints-and-permissions>

Use of this article is subject to the [Terms of Service](#)



Supplementary Materials for

Collective clog control: Optimizing traffic flow in confined biological and robophysical excavation

J. Aguilar*, D. Monaenkova*, V. Linevich, W. Savoie, B. Dutta, H.-S. Kuan, M. D. Betterton, M. A. D. Goodisman, D. I. Goldman†

*These authors contributed equally to this work.

†Corresponding author. Email: daniel.goldman@physics.gatech.edu

Published 17 August 2018, *Science* **361**, 672 (2018)

DOI: 10.1126/science.aan3891

This PDF file includes:

Materials and Methods
Figs. S1 to S26
Tables S1 to S4
Captions for Movies S1 to S5
References

Other Supporting Online Material for this manuscript includes the following:
(available at www.sciencemag.org/content/361/6403/672/suppl/DC1)

Movies S1 to S5

Materials and Methods

1. Ant Experiments

Ten *S. invicta* nests were collected during the spring, summer and autumn of 2014, 2015 and 2016 at the Research and Education Garden of the University of Georgia, GA, USA, and the Chattahoochee-Oconee National Forest, GA, USA. Nest collection and colony extraction were performed according to methods found in (35). Ants were housed in plastic bins for 2–3 months at an ambient room temperature of $23\pm 3^{\circ}\text{C}$ with a relative humidity of $30\pm 2\%$, and fed *Vespula* larvae and supplied with tap water twice a week.

1.1 Primary Ant Digging Experiments

Small groups of 30 ant workers from the laboratory-housed colonies were isolated in transparent containers filled with simulated cohesive soil made of 0.25 mm diameter wetted glass spheres (Ballotini glass particles). The experiments were conducted for 48 hours in $W=0.01$ and $W=0.1$ wet soils (3 trials for each soil moisture). All the experiments were repeated for 3 different colonies. The abdomens of the workers were marked in different colors. A plastic insert separated ants from cohesive soil and featured a single entry point next to the transparent wall of the container. A small (~ 5 mm) indentation was made next to the transparent wall of the container to prompt excavation. In each experiment, ants constructed a single tunnel. The top portion of the container was used by the ants for excavated soil deposition.

The container was fixed on the motorized stage and the camera was focused on the first 2 cm of the tunnel at a distance of approximately 3 ant body lengths. As the tunnel grew in length, the relative positions of the tunnel and the camera were adjusted such that the tip of the tunnel was always visible. The camera was streamed, during which real-time processing detected the presence of ants based on pixel intensity. When an ant entered the camera's field of view, the camera was triggered to record 60 seconds of video at 15 fps.

Work among excavators was characterized by manually counting the number of occurrences in which an ant visited the tunnel. Ants were classified as visitors if they appeared within the camera's view of the tunnel at any point within the duration of the experiment. Non-visitors were those ants that were never detected by the camera. Lorenz curves described the workload distribution by linking the cumulative share of visiting workers in the population (ranged from the least to the most hardworking individuals) to the cumulative share of work performed by the excavating group.

The Gini coefficient (a measure of statistics dispersion) (15) derived from the shape of the curve reflected the inequality in the workload distribution within visiting group. In general, when the Gini coefficient is close to 0, the effort of the ants during the excavation is nearly equal. In contrast, a Gini coefficient close to 1 indicates highly unequal workload distribution with a few active diggers in the visiting group carrying out the bulk of the workload. To calculate the Lorenz curves and Gini coefficients of the 48-hour experiments, the only ants that were included were those that were detected as having visited at least once during those 48 hours. To calculate the Lorenz curves and Gini coefficients for 12-hour epochs within those 48-hour experiments, we only considered the ants that visited within those 12-hour time-frames. This ensured that the calculated workload distributions only ever considered the working population of that measured time-period. Note that visitors, which did not successfully dig and reversed without a pellet were also counted in the excavation effort, because non-excavating visitors still expend energy in an excavation attempt and contribute to tunnel traffic. The 48 hour experiments revealed no significant effects of epoch (1-way ANOVA $F_{3, 20}=0.85$, $p=0.48$) or soil wetness W (1-way ANOVA, $F_{1, 23}=2.54$, $p=0.13$)

on the Gini coefficients obtained from Lorenz curves. Similar workload inequality characteristics are observed from the first 3 hours, by which point the tunnel length has typically not yet exceeded 2 cm. A summary of Gini coefficients extracted from the experiment is provided in Table S1.

1.2 Active Removal Ant Experiment

To determine how the removal of top 5 most active diggers from the colony affects the workload distribution and efficiency of tunnel construction, groups of 30 ants were set to excavate cohesive granular media. Rarely, an ant would lose its colored marker during the experiment, appearing indistinguishable from the black marked ant in the camera. Thus, to avoid misidentification, instead of tracking all 30 ants, we omitted the ant marked black from analysis. The excavation process was recorded for 3 hours. The ants were removed from the container and set to rest for at least 12 hours. The recorded data was analyzed to determine the 5 excavators that most contributed to tunnel construction. These active excavators were removed from the group and the experiment was repeated for an additional 3 hours. The rates of tunnel construction and the Gini coefficients were measured and compared for the first (before removal) and the second (after removal) parts of the experiment. The results were obtained in the experiments with three different colonies and averaged.

Tunnel construction rates varied little between the two phases of the experiment. In fact, the individual growth rate increased slightly: 0.58 ± 0.2 mm/ant within the first part of the experiment versus 0.67 ± 0.3 mm/ant in the second part. The workload distribution also did not change and the Gini coefficient was 0.73 ± 0.15 for control (first phase of experiment) and 0.62 ± 0.06 for active removal (second phase), see Table S2. After the most active excavators from the first part were removed, several idle diggers increased their contribution to the excavation task. The contribution of the most active excavators within the first and the second parts of the experiment was comparable: $74 \pm 21\%$ versus $74 \pm 5\%$ of all observations in the tunnel. The most active diggers of the second part of the experiment had contributed to only $10 \pm 11.4\%$ of total observations (546 ± 65.8) during the first part of the experiment. Thus, individual ants were able to modify their behavior in response to the changing traffic dynamics of the tunnel.

1.3 Calculation of tunnel-width normalized ant occupancy

The control experiments from the active removal experiments were used for calculating tunnel-width normalized ant occupancy, $\bar{\lambda}$ ((average number of ants in the tunnel)/(tunnel width)). Each frame in the video ($15\text{fps} \times (60 \times 60 \times 3\text{s}) = 162000$ frames) was analyzed in MATLAB to identify each colored ant using image processing techniques. The number of color blobs identified in each frame was representative of the number of visiting ants in that particular frame. The tunnel width was approximated to be 2 ant body widths (BW) following results from a previous study (20). The occupancy was then temporally averaged over 3 minutes chunk ($15\text{fps} \times (60 \times 3\text{s}) = 2700$ frames) at 3 different time points in the experiment. This was repeated for 3 different experiments and the average experimental ant occupancy across these experiments is projected on the fundamental traffic diagram in Fig. 3E with shaded areas representing standard deviation from 3 experiments.

1.4 X-Ray reconstruction of ant nest

A colony of *S. invicta* fire ants excavated a 3D nest in a 25 cm wide cylindrical container filled with $240\text{--}270\text{ }\mu\text{m}$ glass beads over the course of a week. The nest was then X-ray scanned (135 keV, 2.5 mA) and CT reconstructed in 3D (Fig. 1A).

2. Cellular automata model

We used a cellular automata model to elucidate the effects of collective actions on traffic during tunnel construction. In a rectangular tunnel lattice, each cell could take one of four possible states: soil, empty/excavated space, ascending excavator, and descending excavator. The initial conditions of the simulation included the number (n) of ants excavating in a group each with body length, BL , and body width, BW , as well as the width of the tunnel (W_T), the initial length of the tunnel, and the protocol of social organization of the group. At every simulation step, the ant was characterized by its 2D position (x,y), the direction of motion, whether or not they were carrying a pellet, and probability P to return back to the tunnel after pellet deposition.

The state of the cells in the model changed by a discrete time step according to a simple set of rules. At each iteration step, a CA ant located in the tunnel moved one CA cell forward or diagonally forward (“walked”) with a probability p unless the destination cell was occupied. This probability affected the duration of ant clusters and was chosen from experimental observations (9). Also, when in a cluster, a descending ant had a probability to turn back and exit the tunnel without excavation (“reversal”). Due to the geometrical constraints of the CA model, the reversal behavior was an essential to prevent jamming for infinitely long times for populations $n > 2 \cdot W_T / BW$. In the absence of the reversal behavior, unresolvable clogs consisting of $n \geq 2 \cdot W_T / BW$ ants may form which span the width of the tunnel and disrupt the excavation process. Thus, reversal behavior was implemented for all CA simulations regardless of workload distribution.

When the ant reached the tip of the tunnel, it spent several time steps excavating. The excavated pellet was transported to the entrance of the tunnel and expelled from the tunnel (“pellet deposition”). After a predefined number of pellets were collected the tunnel grew in length by 1 cell. After pellet deposition, the ant would return to the tunnel with probability P or switch to resting mode. During the pellet deposition or resting mode, the ant was neither contributing to the excavation, able to cause clogs, nor increasing tunnel density. The exit from the resting mode was also defined by probability P .

The unequal workload distribution was achieved by introducing the probability, P , to return to excavate in the tunnel after a pellet deposition. To simulate fully active ants, workers attempted to reenter the tunnel immediately after pellet deposition ($P = 1$). In groups with unequal workload distributions, the probability of the ant to return to try and return to the tunnel was unique, fixed and derived from the experimental ant workload distribution measurements as $P(\frac{n_i}{n}) = f(\frac{n_i}{n}) - f(\frac{n_i-1}{n})$, where n_i was the number of ants in a sequence from the least to the most active; n was the excavating group size, and f was a Lorenz function.

All parameters describing ant behaviors were found via experimental observation; the only parameter varied to allow the system to match experiment was the excavations to grow tunnel size by 1 cell. The rates were calculated from the slope of the tangential lines fitting the initial portion of the tunnel growth curve. The tunnel excavation rates in simulations differed greatly depending on excavation scenario. In general, the groups of active diggers ($P = 1$) were most efficient when the number of excavators in the group was small. The increase in the number of active excavators led to the formation of ant clusters, which eventually slowed the nest construction down. The unequal workload distribution $P(\frac{n_i}{n})$ in large groups of excavators allowed for reduction of ants density in the tunnel throughout the experiment and, thus, produced high nest construction rates

even when the number of diggers in the excavating group was large. In large groups of diggers with unequal workload distributions, the excavation rates were insensitive to the addition of excavators.

2.1 Occupancy and flow in CA model

The CA simulations were carried out for ant groups of different sizes. The width-normalized ant occupancy and the flux were measured in $L_T = 5$ cell long tunnel (~ 2.5 cm actual length). The flux and occupancy were measured at $i = \text{floor}\left(\frac{L_T}{2}\right) + 1$ position in the simulated tunnel (Fig. S4). We calculate ant occupancy as the time-averaged number of ants in the tunnel divided by the tunnel width, W_T , in ant body widths, BW :

$$\bar{\lambda} = \frac{1}{T} \sum_{t=1}^T n_i(t) / W_T \quad (1)$$

where $n_i(t) = 1$ if the site is occupied at time t and 0 otherwise. Occupancy at a fixed site i was averaged over a time period $T=3$ hours. The average bi-directional flux \bar{q}^T between site i and neighboring sites $i + 1$ and $i - 1$ was defined as

$$\bar{q} = \frac{1}{T} \sum_{t=1}^T [n_{i,i+1}(t) + n_{i,i-1}(t)] / W_T \quad (2)$$

where $n_{i,i+1}(t) = 1$, if the ant moved between sites i and $i + 1$, and $n_{i,i-1}(t) = 1$ if the motion occurred between i and $i - 1$, and zero if the motion was not detected. The flux was averaged over time T corresponding to 3 hours of experiment. The flux was normalized by the tunnel width.

We introduced these definitions to compare traffic in groups of different sizes governed both equal and unequal workload distributions. The fundamental flow diagrams (tunnel flow \bar{q} vs occupancy, $\bar{\lambda}$) for each experimental condition are provided in the main text.

2.2 Clustering characterization in CA model

The implementation of unequal workload distribution reduces the immediate density of the ants in the tunnel in simulations. As a result, the number of clusters (I_c), their spatial extension (a_n) and time duration (T_c), as well as the number of ants involved in the jams C decrease, allowing for stable traffic formation (Fig. S5).

To analyze traffic, the jam was defined as agglomerations of 2 or more ants located in the neighboring cells at a simulation step k . The number of clusters was defined as the total number of agglomerations observed over 50,000 simulation steps. Each simulation step was considered independently. The site occupancy time T_c was defined as the time it takes for a particular cell occupied by an ant involved in a jam to change its value from “occupied” to “vacant”. The average spatial extension of the jam was defined as the number of cells occupied by the ants sequentially along the tunnel length. The number of ants involved in a cluster, the site occupancy time and the spatial extension of a jam were averaged over all simulation steps and results are reported on Fig. S5.

2.2.1 Cluster Size and Frequency Dynamics in CA model

We characterized how cluster severity was affected by reversals and unequal workload distributions through an analysis of cluster formation. Clusters in 30-ant simulations were identified at each simulation time point and categorized by the number of CA ants that comprised the cluster. Any group of ants that blocked the entire tunnel width was considered a cluster. We

found a prevalence of large clusters for extremely low reversal probabilities in both equal (*Fig. S26 A*) and unequal (*Fig. S26 B*) workload distributions. A minimal increase in reversal probability reduced the prevalence of the largest clusters from forming. However, even accounting for higher reversal probabilities, equal workload distributions resulted in wider distribution of cluster sizes, whereas the optimized workload distribution produced a sharper concentration of small clusters, which were more easily dispersed. Thus, cluster mitigation is most effective using both reversals and unequal work probabilities in combination.

2.3 Optimal distributions CA using a genetic algorithm

A genetic algorithm (GA) was used to search for entrance probability distributions that produced optimal digging rates. The GA is a biologically inspired optimization technique used typically to find solutions where the parameter space is large. GAs modify or evolve populations of solutions at each generation, through processes known as reproduction and mutation, towards the optimal solution. Each probability distribution for a single simulation is known as a “chromosome”, and each probability for a single ant are called “genes”. The set of all chromosomes at each generation is called a population. The reproduction phase requires each chromosome to be run, and depending on the output of the objective function, the metric by which each chromosome is measured, certain chromosomes are selected to be parents for the next generation. Our implementation used the digging rate as the objective function. The best performing chromosomes, known as the elite percent go unchanged to the next generation. The rest of the chromosomes are paired up, and a percentage, known as crossover percentage, are crossed over. Crossover is where a random site is chosen along the length of a chromosome and the genes of the paired chromosomes are switched around that point. After crossover, all genes belonging to the non-elite group of chromosomes have a chance, known as mutation probability, to be assigned a new random value. This helps to mitigate chances of becoming stuck in local minima (or maxima) of the optimized quantity.

We used MATLAB’s genetic algorithm toolbox (36). Our selection type was the default used in MATLAB’s GA toolbox, stochastic uniform. The specific values for our reproduction and mutation rates were as follows: 5% for the elite selection, 0% for the crossover fraction, and a variable number of gene was subjected to mutation according to an adaptable mutation rate, the default option for MATLAB. We used a population size of 200 probability distributions per generation, and ran 50 generations.

2.4 One at a Time (OAT) Model

2.4.1 Introduction

We model a tunnel as a one-dimensional lattice of Z sites; an ant occupies one lattice site. The tunnel has an open boundary at the left (site 0) where ants can enter and exit, and a closed boundary at the right (site N) that represents the end of the tunnel. Note that for simplicity we keep N fixed: in this model, the tunnel does not change length in time.

Each ant can move toward to the next site at rate v . Ants enter the tunnel at rate αv , which may be the same for each ant or variable. Once an ant enters the tunnel it moves to the right at rate v , but can reverse and move to the left. If an ant is blocked by another ant in front of it, it cannot move. Ants reverse at rate S either when they reach the end of the tunnel, or when they are adjacent to another ant going the opposite direction. At site 0 in the tunnel, ants moving to the left exit with rate βv .

Once an ant reaches the end of the tunnel (site Z), reverses, goes back, and exits the tunnel, it

completes one cycle of digging. Since the model only allows one ant to occupy a given site (ants sterically exclude each other), the ant that completes a digging cycle is the first ant to enter the tunnel when it is empty. The ants that follow only hinder the digging process. We call this the *One-at-a-Time (OAT) model* (Fig. S13).

We define excavation rate in this model as the number of completed digging cycles over a certain time. We used kinetic Monte Carlo (kMC) simulation (see section 2.4.4 for details) methods developed in our previous work (25) to do simulations of this model. In simulations, we measure the total number of ants, and count events in which the tunnel has no ants in it. Model parameters that produce higher excavation rate lead to more events during which the tunnel is empty (Fig. S14).

If the inward flux leads to a time between ants entering the tunnel that is longer than the time for an ant that has already entered to reach the end of the tunnel and exit, then increasing α increases the excavation rate. However, if the time between ants entering is shorter than the digging time, most ants that enter the tunnel create traffic jams that block the digging ant from retreating. This decreases the excavation rate. Simulating the OAT model at different values of α (whereby all ants in a simulation are given an identical α) results in an intermediate peak in excavation rate as a function of α (Fig. S15). Giving all excavators an identical α is akin to the equal workload distribution in Active ants of the CA model, whereby varying α modulates the overall level of activity of all ants.

We analytically derive the excavation rate by estimating the typical time of one digging cycle. The time to complete one cycle is the sum of (a) the time for the first ant to enter the tunnel, (b) the time it takes for the digging ant to walk to the end of the tunnel and back to the entrance, and (c) the time required for all ants in the tunnel to reverse their direction. The typical time to wait for the first ant to enter the tunnel is $1/\alpha v$, the inverse of the entry rate. The typical time for an ant to walk to the end of the tunnel and back is $2L_T/v$, where L_T is the length of the tunnel. The additional time due to waiting for ants to reverse direction we estimate by noting that the typical reversal time is $1/S$. If the tunnel were infinitely long, then the typical distance between two ants in the tunnel would be the typical time between ants entering the tunnel times the typical speed of an ant, which is $1/\alpha v \times v = 1/\alpha$. However, because the tunnel is not infinite, this distance is reduced by the ants that change direction. The typical distance an ant moves during a switching event is v/S . Thus, on average, the ant moving forward and the switching ant will meet when they each have traveled half of the distance between them, $1/2 (1/\alpha - v/S)$. This is the typical distance that an advancing ant moves before switching because it hits another ant. This must be scaled by L to account for all the ants in the tunnel, and an additional time of $1/S$ must be added to account for the first ant to reverse at the end of the tunnel. The overall time of a digging cycle (Fig. S20) is thus:

$$T = \frac{1}{v\alpha} + \frac{2L_T}{v} + \frac{1}{S} \left(\frac{L_T}{\frac{1}{2}(\frac{1}{\alpha} - \frac{v}{S})} + 1 \right) \quad (3)$$

Note that disagreement between the theoretical curve and the kMC simulation (Fig. S15) occurs for relatively short tunnels when there are large jamming effects: in our model, we didn't consider the size of the ants and the longest distance an advancing ant could move. Note as well that our model becomes ill defined when $v/S > 1/\alpha$, because the term in the denominator becomes negative. This occurs for small S , which physically occurs when reversal is so slow that the

excavation rate is dominated by waiting for reversals to occur. If the switching rate at the end of the tunnel has a unique rate, g , the rate at which an excavator completes an excavation, the overall time of a digging cycle becomes:

$$T = \frac{1}{v\alpha} + \frac{2L_T}{v} + \frac{1}{s} \left(\frac{L_T - \frac{1}{2}(\frac{1}{\alpha} - \frac{v}{g})}{\frac{1}{2}(\frac{1}{\alpha} - \frac{v}{s})} + 1 \right) + \frac{1}{g}. \quad (4)$$

2.4.2 Training an unequal workload distribution

The above model assumes that every ant has the equal workload α , and demonstrates that the excavation rate actually deteriorates if ants are too diligent (large α). This suggests that system excavation rate might be sensitive to the workload distribution. We implemented a training algorithm with the following rules:

1. The total number of ants is fixed.
2. If an ant completes a digging cycle after it goes into the tunnel (in other words, it reaches the end of the tunnel), then it increases its workload, α , by a factor of q ($\alpha_{new} = q\alpha$).
3. If an ant enters the tunnel but is hindered (i.e., it reverses before reaching the end), it decreases its workload by a factor of q ($\alpha_{new} = \alpha/q$).
4. There is a maximum workload α_{max} , which is necessary to prevent super-diligent ants from taking over all the work.

In our simulation algorithm, each ant has equal probability to be selected to *attempt* to enter the tunnel, but the i th ant has its own probability α_i to decide if it “wants” to enter or not.

Using these above rules to train simulated ants in our model, we find nearly identical workload distributions (Lorenz curves), Gini coefficients (Fig. S16), and digging rate (Fig. S17), regardless of α_i for the population. The workload distribution of the trained ants is unequal; the Lorenz curves reveal that only about half of the ants are working, while the others are idle. Further, the populations reliably converge to their final workload distribution rapidly (Fig. S23). Since traffic jams in the tunnel are controlled by the total number of ants, the model predicts that (a) a larger ant population results in a more idle ants and a higher Gini coefficient (Fig. S18), and (b) the higher the maximum workload α_{max} , the higher the Gini coefficient (Fig. S19). This occurs because the overall work has a maximum, and more working ants won't increase the work. Thus, the optimal scenario in this model is for one ant to do all the work by returning into the tunnel immediately once it goes out (i.e., $\alpha_{max} = \infty$).

2.4.3 Occupancy and flow in the OAT model

The time-and-spatial-average occupancy, $\bar{\lambda}$, (average occupancy) and the time-average flow, \bar{q} , (average flow) in the OAT model are similar to (23):

$$\bar{\lambda} = \frac{1}{T} \sum_{t=1}^T n_i(t) \Delta t \quad (5)$$

$$\bar{q} = \frac{1}{T} \sum_{t=1}^T n_{i,i-1}(t), \quad (6)$$

where $n_i(t)$ is 1 (or 0) if the site is occupied (or unoccupied) at time t at site i , and $n_{i,i-1}(t)$ is 1 (or 0) if the ant moved (or didn't move) between site i to $i - 1$. The parameter Δt is 1 and $\sum_{t=1}^T \Delta t = T$. Measuring occupancy at the midpoint of the tunnel ($i = L_T/2$) yields:

$$\bar{\lambda} = 2 \frac{\left(\frac{L_T}{2} - \frac{1}{2(\frac{1}{\alpha} - \frac{v}{S})} + 1 \right)}{v} \left[\frac{1}{v\alpha} + \frac{2L_T}{v} + \frac{1}{S} \left(\frac{L_T}{2(\frac{1}{\alpha} - \frac{v}{S})} + 1 \right) \right]^{-1} \text{ or} \quad (7)$$

$$\bar{\lambda} = 2 \frac{\left(\frac{L_T}{2} - \frac{1}{2(\frac{1}{\alpha} - \frac{v}{g})} + 2 \right)}{v} \left[\frac{1}{v\alpha} + \frac{2L_T}{v} + \frac{1}{S} \left(\frac{L_T - \frac{1}{2(\frac{1}{\alpha} - \frac{v}{g})}}{\frac{1}{2(\frac{1}{\alpha} - \frac{v}{S})}} + 1 \right) + \frac{1}{g} \right]^{-1}, \quad (8)$$

where $\left(\frac{L_T}{2} - \frac{1}{2(\frac{1}{\alpha} - \frac{v}{S})} + 1 \right)$ is the number of ants that pass site $i = L_T/2$. The term $\frac{1}{v}$ is due to the corresponding staying time of an ant that stays in the site i (the length of an ant is the same as the length of a site). The last part of the equation is $1/T$, where T is the digging cycle. The second equality of the equation is the scenario of the unique switching rate at the end of the tunnel.

The average flow depends on the site as well. We defined it at the end of the tunnel, which is the same as the flow of the successfully working ant. The average flow is:

$$\bar{q} = \frac{1}{T} = \left[\frac{1}{v\alpha} + \frac{2L_T}{v} + \frac{1}{S} \left(\frac{L_T}{2(\frac{1}{\alpha} - \frac{v}{S})} + 1 \right) \right]^{-1} \text{ or} \quad (9)$$

$$= \left[\frac{1}{v\alpha} + \frac{2L_T}{v} + \frac{1}{S} \left(\frac{L_T - \frac{1}{2(\frac{1}{\alpha} - \frac{v}{g})}}{\frac{1}{2(\frac{1}{\alpha} - \frac{v}{S})}} + 1 \right) + \frac{1}{g} \right]^{-1}, \quad (10)$$

where the second equality of the equation is the scenario of the unique switching rate at the end of the tunnel. The numerator is 1 since there is only one successfully working ant in a digging cycle. Figures S21 and S22 show the occupancy-flow curves (fundamental diagram) when considering both a unique and identical switching rate for excavation at the end of the tunnel.

Agreement was achieved between the OAT model and the CA simulation for the fundamental diagram. However, some parameter tuning and scaling was required to account for differences between the models. Namely, in the CA model, unlike in the OAT model, not only are there multiple lanes, but CA ants are able to switch lanes to resolve clogs, whereas an ant in the OAT model must exit the tunnel. Additionally, for the flow-rate calculation, the CA model considers the flow of a successfully excavating worker twice, once on the way to excavate and again on the return to deposit. Whereas, in the OAT model, the flow of an excavating worker is considered only once. For fundamental diagram calculations, a tunnel length of 5 was used, as in the CA simulations.

2.4.4 The kinetic Monte Carlo simulation

We performed kinetic Monte Carlo (kMC) simulations of a discrete model with the time step t and the following rules at each time step for a one-dimensional lattice with Z sites:

1. Randomly choose a direction (towards the excavation site or towards the tunnel entrance) and site i .

2. If the site is occupied and the next site in both directions are empty, the ant steps forward with probability $v\Delta t$.
3. If the chosen site is occupied with an ant moving towards the excavation site and the next site over is occupied (or the chosen site is at the excavation site), the ant switches direction with probability $S\Delta t$.
4. If site 1 in the excavation direction is chosen, and it is empty, the ant occupied the site with the probability $v\alpha$.
5. If site 1 in the exiting direction is chosen and is occupied, the ant leaves with the probability $v\beta$ (we set $\beta = 1$ in the simulations).
6. Repeat steps 1-5 $2Z$ times total to sample all sites in both lanes.

The tunnel length is $Z = 20$ in the simulations (unless otherwise stated). We typically choose $\Delta t = 0.005$ such that the speed of the ants is $v\Delta t = 0.3125$ sites per kMC cycle, and $S\Delta t = 0.002175$ per kMC cycles (unless otherwise stated). We ran 6×10^8 kMC cycles per condition (unless otherwise stated). The simulation reaches the steady state typically after 10^6 kMC cycles in the training simulations. We measured the data by averaging the last 3×10^8 kMC cycles. We started the simulations with empty tunnels.

3. Robot Experiments

Robophysical experiments were conducted to test the performance and clustering dynamics of robots following each of three different behavioral protocols. The first strategy (Active, *Fig. S6*) assigned equal maximal attempted activity to all diggers: after soil deposition, each robot immediately returned to the tunnel to excavate. In the second protocol (Reversal, *Fig. S7*) the robots were also programmed to immediately resume excavation after deposition but reversed after some time not being able to reach the excavation site. In the third protocol (Lorenz, *Fig. S8*), we implemented an unequal probability to excavate derived from experimental ant workload inequalities.

Groups of robots operated in simulated environment that consisted of a table top testbed, featuring a quasi 2D tunnel and a pellet deposit area. The pellet deposit area was also used to accommodate inactive robots. The tunnel was partially filled with a cohesive simulated media made of loose rare-earth magnets (BYKES Technologies) contained in 3D-printed plastic shells 1.8 cm in outer diameter. The width of the tunnel allowed for simultaneous side-by-side tunnel excavation by two robots. In our previous laboratory experiments (12), *S. invicta* constructed ~ 1.5 body length wide tunnels

3.1 Robot design

Robots were designed to create an inexpensive yet functional robophysical system which could be used as a tool to study the effect of social protocols on collective excavation in confined spaces. The design of the robotic workers implements readily-available off-the shelf and open-source parts. A list of major components is shown in Table S4 [below, adopted from appendix B (37)]. Discussion of core components below provides insight into robot functionality and capabilities. A maximum of 4 robots was used in the experiments.

3.2 Microprocessors

Each robot utilized an Arduino Due microcontroller to handle sensor I/O, computations, and logic. The microcontroller software was set up to have three user programmable behavioral modes described in the paper: Active (Fig. S6), Reversal (Fig. S7), and Lorenz (Fig. S8). Each item in the flow chart has low-level control schemes responsible for obtaining sensor data, performing state estimation, and controlling the actuators. An Arduino Fio microcontroller was also used to handle data logging. Current, voltage and the state of the behavior mode was recorded and stored on a micro SD card for post processing.

3.3 Sensors

3.3.1 Navigation sensors

A low-cost camera system (Pixy CMUcam5) was used to accomplish most of the navigation. The camera located the simulated pink pheromone trail and supplied the Arduino Due with centroid coordinates and the size of the detected pheromone trail object. A lane following algorithm was used to guide the robot between the excavation and the deposit sites.

A magnetometer further improved navigation. A robot could be pushed off course in the event of a collision with another robot and lose sight of a simulated pheromone trail. The magnetometer would be used to recover correct heading. A priori knowledge of the test bed layout was exploited and thus the robot knew in which direction it needs to orient itself to get towards a current goal. The magnetometer simulated the sense of gravity in animals. A magnetometer was also used in conjunction with a gyroscope to obtain turning feedback. Robots would alter their turning strategy if no progress was measured while attempting to turn around.

3.3.2 Collision sensors

Two short range (15cm) infrared sensors were used to detect objects and obstacles directly ahead. In the event of an obstacle detection, the robot would attempt to steer around. The robot could detect physical interactions with the other robots or the environment using mechanical switches embedded beneath a segmented robotic shell. Each shell segment rested on a mechanical switch which was triggered by physical contacts within the environment. Thus, not only the contact, but also its approximate direction was sensed.

3.3.3 Environment manipulation sensors

An infrared proximity sensor was mounted near the robotic gripper. The sensor was occluded in the event of a successful collection of model media making this event distinguishably recognizable. The same sensor was also used to trigger excavation behavior.

3.3.4 Power management sensors

A bidirectional current sensor, along with a battery voltage level sensor were used to monitor power consumption. The robot relied on these sensors to determine if it needs to get to the charging station and recharge its single cell 3.7V Li-On battery.

3.4 Actuators

The robot locomotion was enabled by a differential wheeled drive system. The robot could drive with speeds up to 18cm/s. Two servo motors were used to operate a robotic arm used for manipulation of the simulated granular media. One servo motor actuated a robotic gripper while the other motor could raise or lower the pitch of the arm.

3.5 Mechanical Design

Figure S9 illustrates mechanical design. The robot's body was made with parts manufactured with a 3D printer. The design was modular, allowing easy access to and replacement of components. Most of the electronics (microcontrollers, power circuits, etc.) were safely hidden inside the robotic shell because the robots were expected to engage in many physical contacts.

3.6 Robot Tracking

The robots were tracked via an image intensity threshold routine (Fig. S10). For each experimental trial, an overhead camera recorded the tunnel area for about 30 minutes at 10 frames per second. For a given frame of video, the image was subtracted from an averaged background image. A threshold was then applied to identify pixels corresponding to the robots. Initial robot positions were manually approximated at the beginning of the video. The robot pixels were then divided into different regions using Voronoi cells generated with the initial robot position. The centroids of these regions were then used to recalculate the robot positions, which were subsequently used as approximations for the next frame.

3.7 Global Traffic Analysis

Excavation rate and energy expenditure were measured for excavation trials (3 trials of each experimental condition) of 2 to 4 robots and 3 different protocols as described in the beginning of supplemental Section 3. Each digging strategy produced distinct trends in tunnel density and energy expenditure (Fig. S12 B). The Reversal strategy exhibited peak excavation performance with two robots, and monotonically increasing density and energy cost for trials with more diggers. During Active strategy trials, robots would clog more frequently at the excavation site with addition of a fourth robot, resulting in a dramatic decrease in tunnel density and increase in energy expenditure. While dynamically allocating tasks through local feedback (38) or even controlling for equal workload (39) have proven useful in achieving robotic swarming goals such as foraging and construction, the simple Lorenz strategy was effective in lowering tunnel density and energy cost. Therefore, particularly for large populations, simply modulating the distribution of individual work effort and likelihood of giving up in the face of traffic jams are effective strategies in targeting optimal traffic densities.

3.8 Local cluster relaxation times

Tracking data was used to identify clusters of robots, defined as groups of robots whose center positions were within a robot length's proximity of each other. Robot lateral positions were represented as intensity potentials in a space-time intensity map, I (Fig. S12 A). Each robot was given a lateral intensity potential function (a half-cycle sine wave with one body length half-period was chosen) centered at the robot's lateral position. Clusters were identified as contiguous potentials. The local dynamics of these clusters were evaluated using a technique often used to study dynamic heterogeneities in non-biological active matter (40). At each time step, clusters were identified and evaluated using a correlation function derived from PIV cross-correlation techniques (41):

$$q(\tau) = \frac{\sum_{x_1}^{x_2} (I(\tau, x) - \bar{I})(I(0, x) - \bar{I}_0)}{\sqrt{\sum_{x_1}^{x_2} (I(\tau, x) - \bar{I})^2 \sum_{x_1}^{x_2} (I(0, x) - \bar{I}_0)^2}}. \quad (11)$$

The correlation overlap function, $Q(\tau) = \langle q(\tau) \rangle$ (where the brackets indicate a time average from time, $t = 0$ to τ , whereby $t = 0$ corresponds to the time step in which the cluster is identified),

compares the spatial overlap of an aggregation (or cluster) at a specific time to the overlap of the aggregation's original lateral segment at a later time, τ (Fig. S12 B).

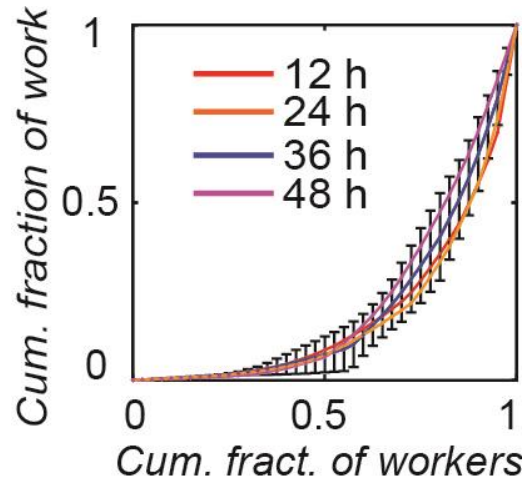


Fig. S1. Experimental Lorenz curves of ant workload distribution for individual 12-hour epochs of 48-hour trials. Error bars indicate standard deviation from multiple trials averaged over 6 trials (3 trials in ~ 0.25 mm diameter glass particles at $W=0.1$ moisture content and 3 trials in $W=0.01$).

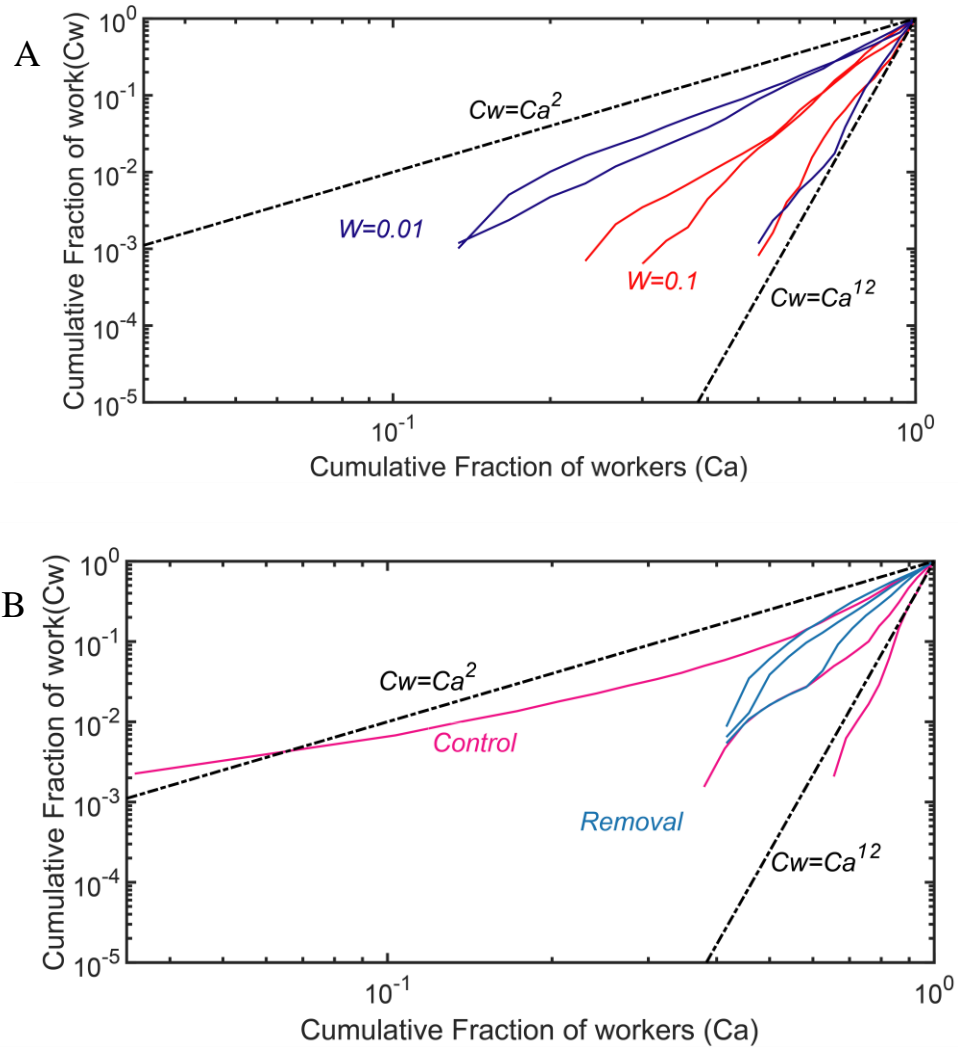


Fig. S2. Log-Log plots of Lorenz curves representing workload distributions in ant experiments (A) for different moisture contents and (B) for active removal experiment. Black dashed lines are power-law curve

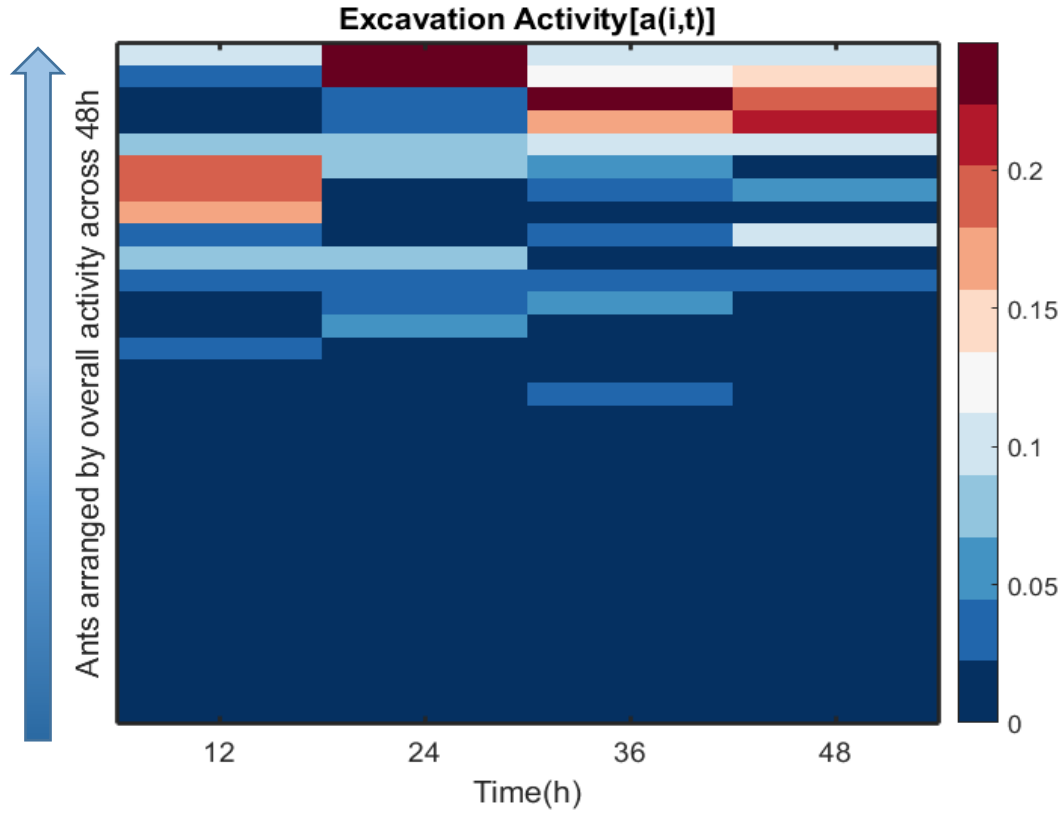


Fig. S3. Dynamic activity pattern of individual ants over different time epochs. The ants are arranged by their overall activity for 48-hours descending from bottom upwards. Excavation activity, $\mathbf{a(i,t)}$ is the number of tunnel visits per 12-hour epochs for an ant \mathbf{i} divided by the total number of tunnel visits within that epoch.

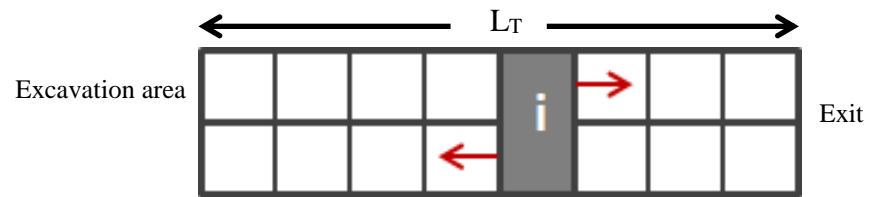


Fig. S4. Schematic of the tunnel in CA model. The occupancy of ants and the flux in the tunnel were measured at the highlighted cell i . The possible directions of ant motion are shown with red arrows.

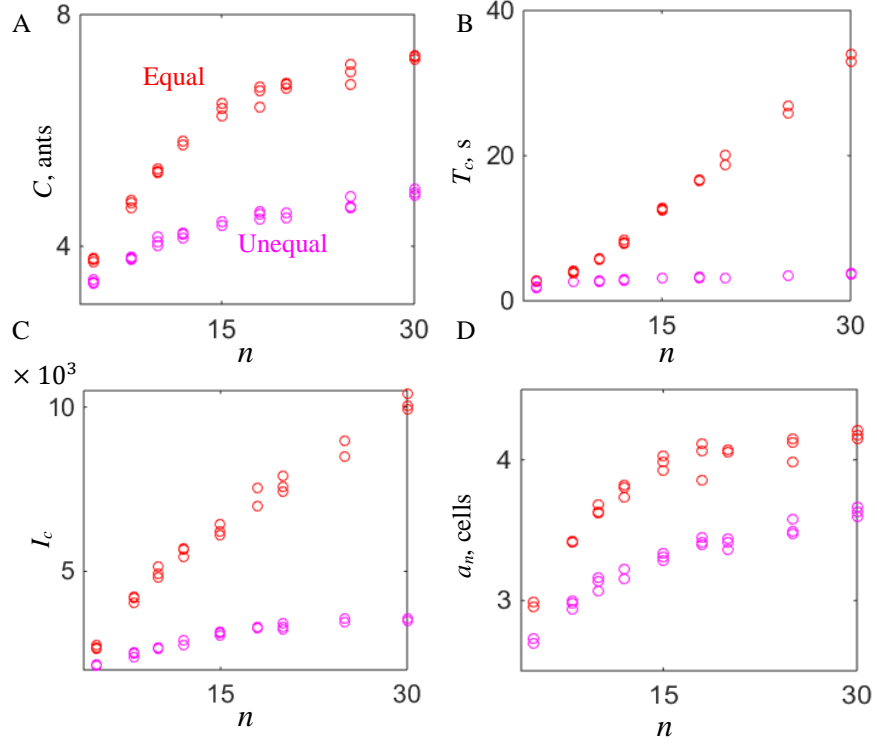


Fig. S5. Simulation results: Average number of ants involved in a jam C (A), site occupancy time T_c (B), total number of jams I_c over 50000 simulation steps (C), and average spatial extension of the jam a_n (D) plotted versus the size of the group for groups governed by equal workload distribution (red) and unequal workload distribution protocols (magenta).

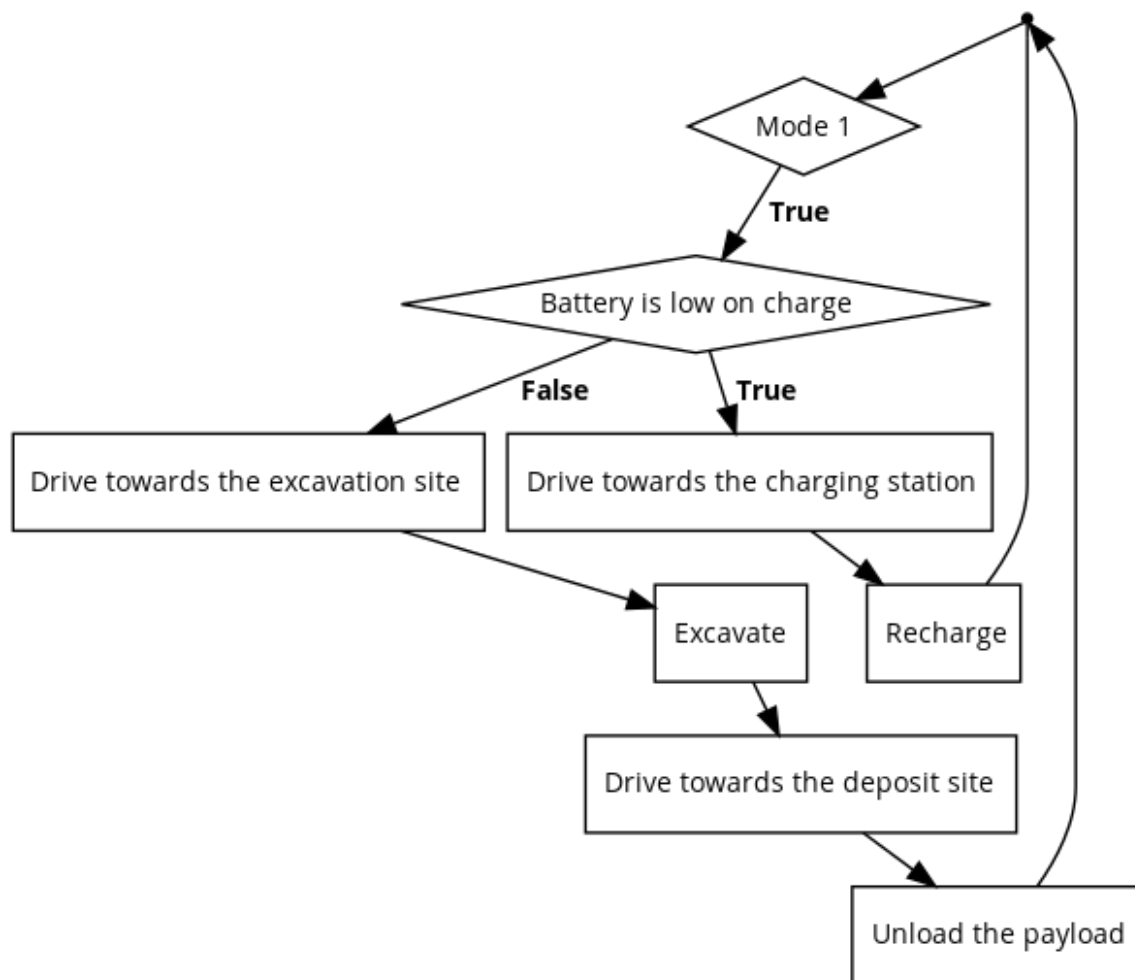


Fig. S6. Active logic flow chart.

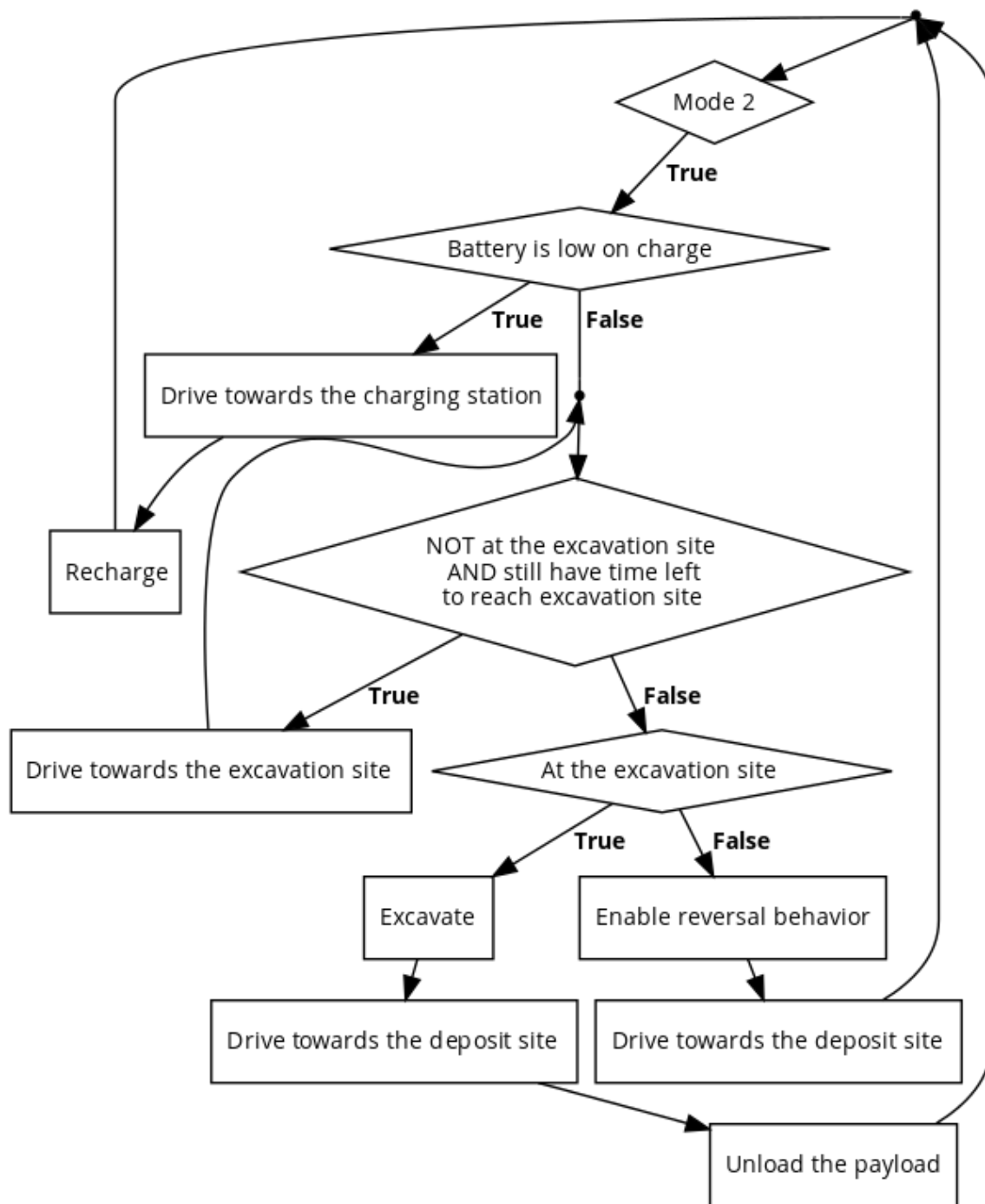


Fig. S7. Reversal logic flow chart.

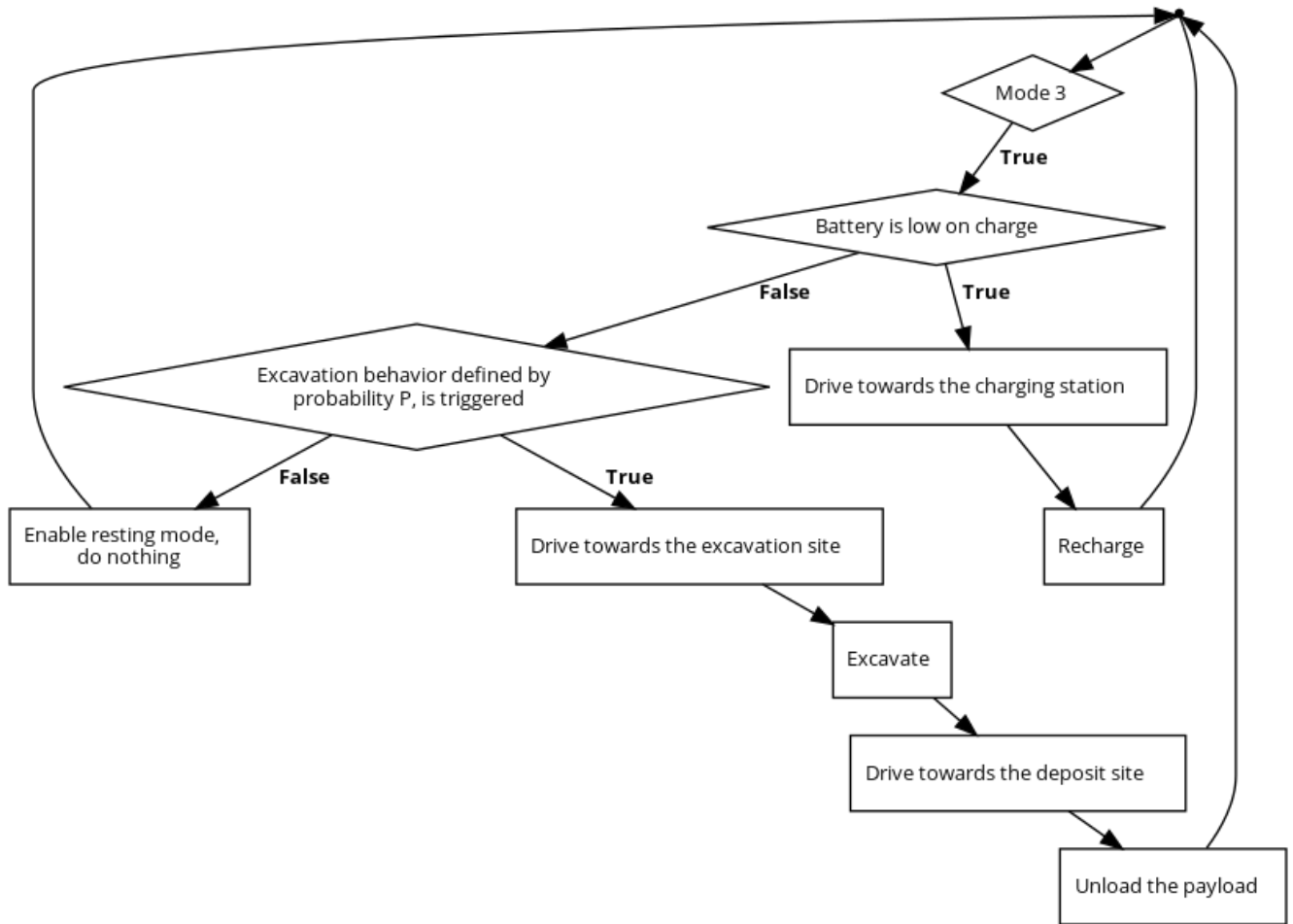


Fig. S8. Lorenz logic flow chart. Note that this logic is identical to Active if $P=1$. Otherwise the robot has a chance to enter resting mode outside the tunnel which last for a specified amount of time.

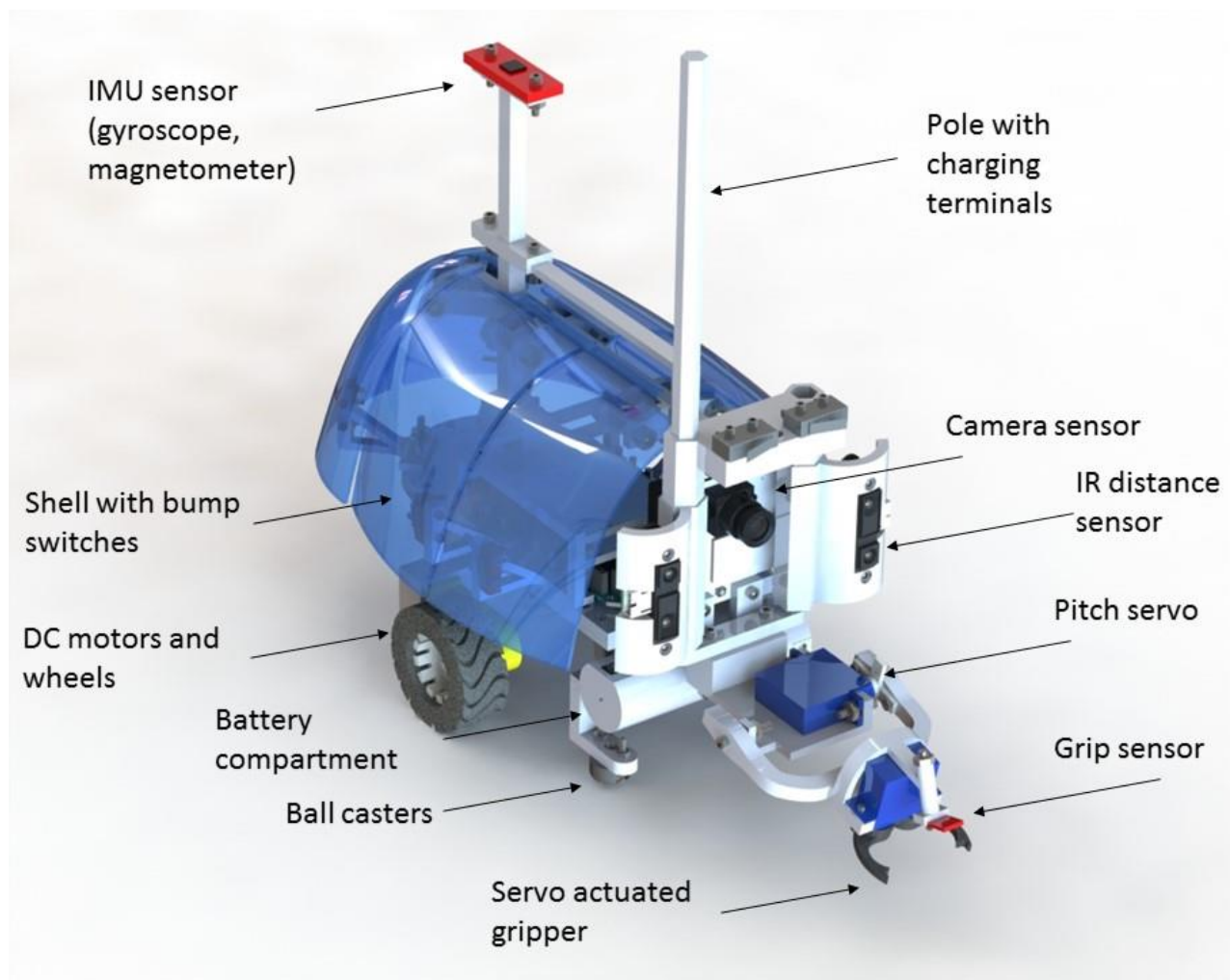


Fig. S9. Mechanical design of robots. Microcontroller and circuitry are inside the shell

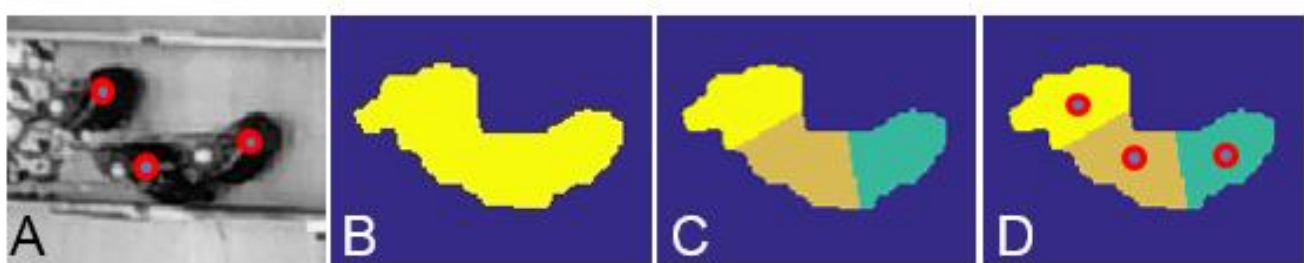


Fig. S10. Robot tracking routine. (A) Initial position estimates. (B) Threshold of background-subtracted image. (C) Voronoi divided robot regions. (D) Centroid calculated positions.

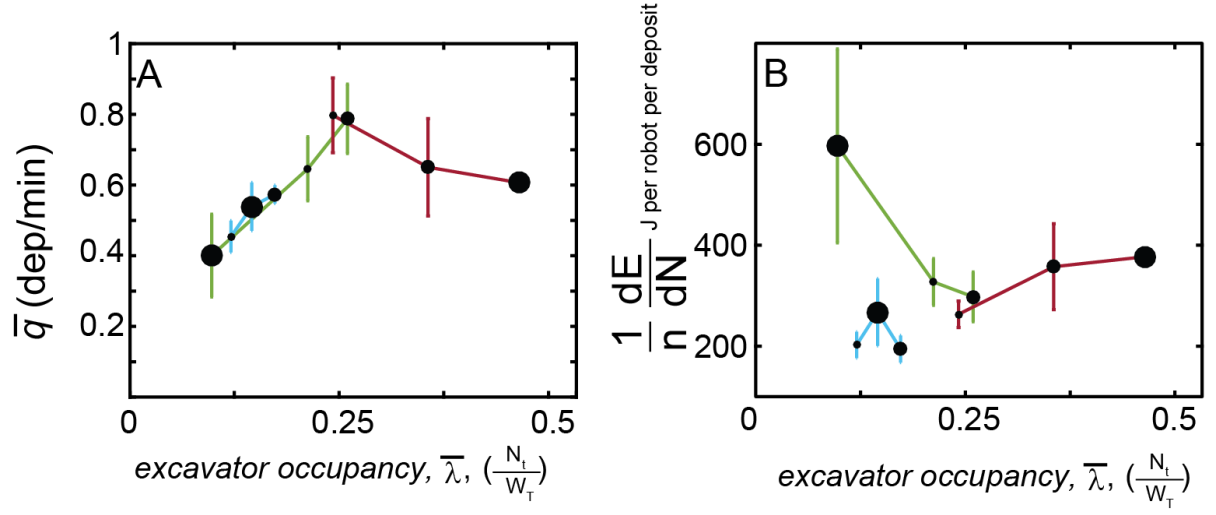


Fig. S11. Robot performance for 2 (smallest marker) to 4 (largest marker) robots using the Active (green), Reversal (maroon) or Lorenz (light blue) protocol. (A) Fundamental diagram; excavation rate, \bar{q} , vs excavator occupancy, $\bar{\lambda}$, where N_t is the number of robots in the tunnel area and W_T is the width of the tunnel area in robot body widths, RW . (B) Energy expenditure vs tunnel density.

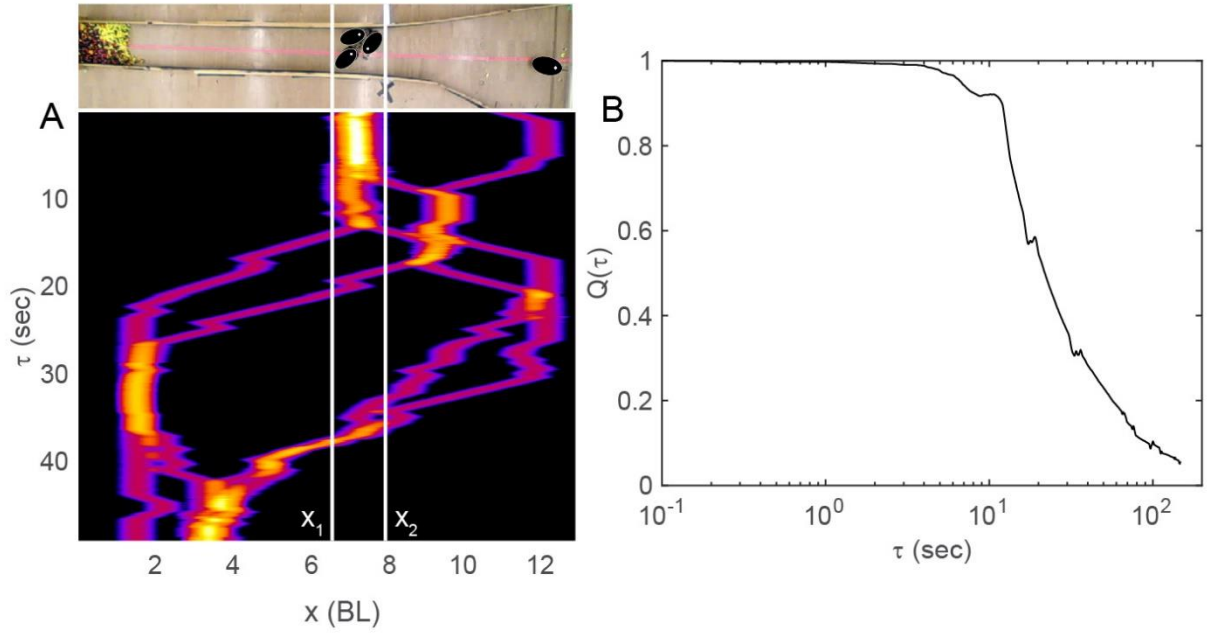


Fig. S12. Analysis of local robot clusters. (A) Sample space-time intensity map. (B) The correlation function $Q(t)$ is calculated from the 3 robot cluster in the first frame in (A) (top panel) using image correlation algorithms used in PIV (41).

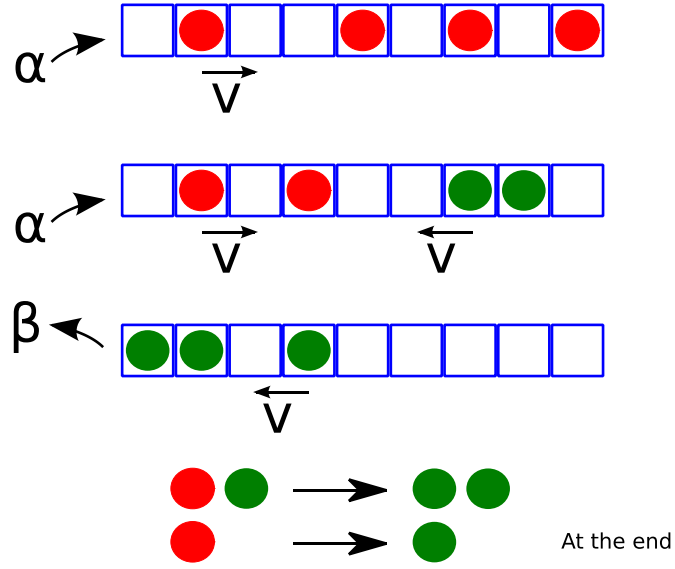


Fig. S13. Schematic of the OAT model. The red circles indicate ants moving to the right, and green moving to the left. Only one ant can occupy each site. Red ants reverse (switch to green) if they meet another green ant in front of them in the direction they move, or if they reach the end of the tunnel. The inward flux is α , which controls the average occupancy at site 0, and β is the exit rate.

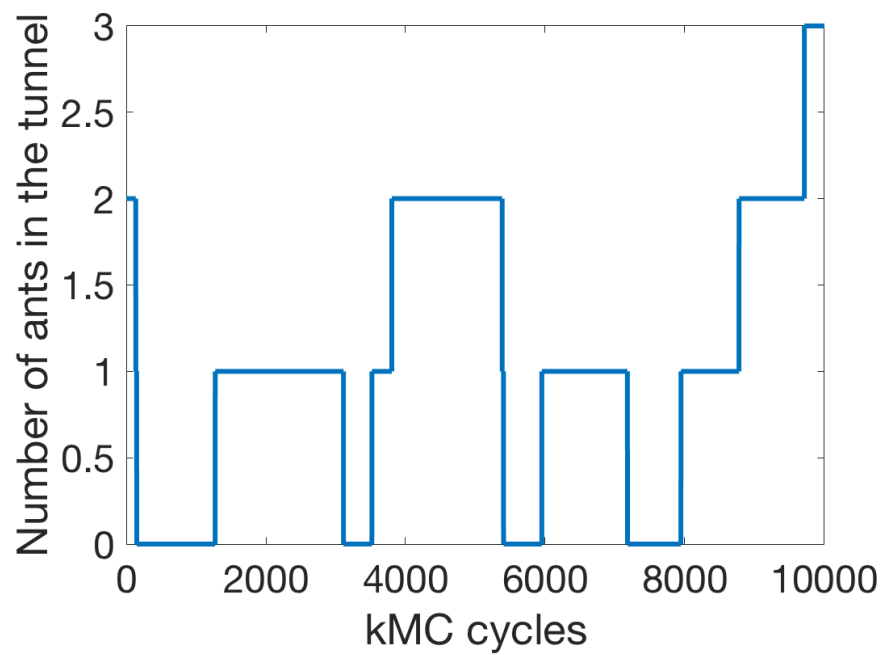


Fig. S14. Results of a simulation showing the total number of ants in the tunnel as a function of time. In this portion of the simulation, three complete digging cycles occur, because the tunnel is empty four times).

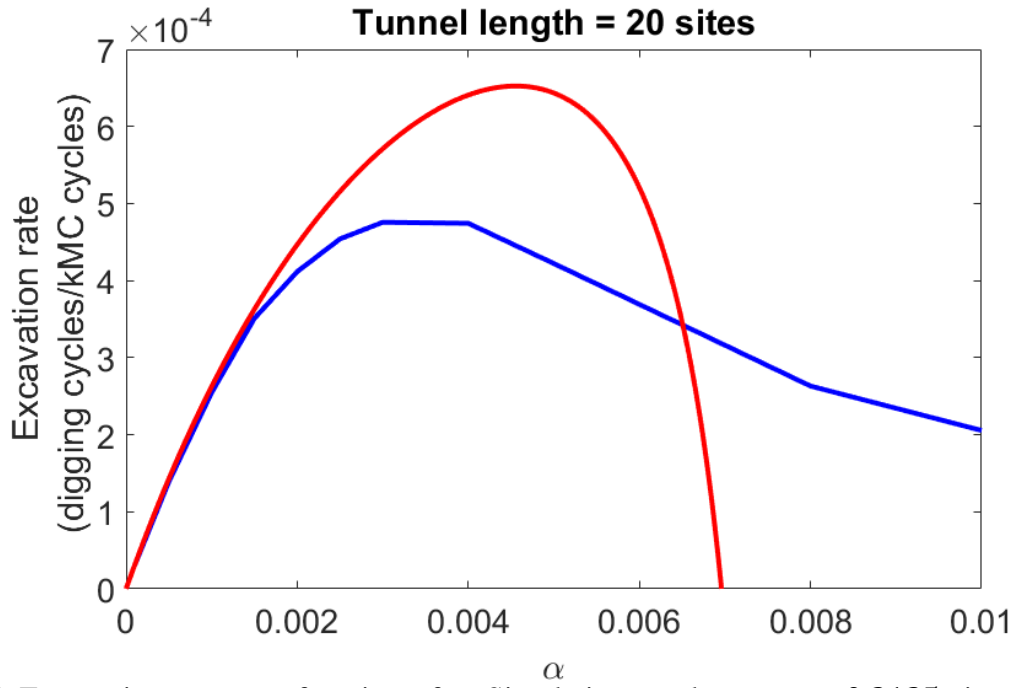


Fig. S15. Excavation rate as a function of α . Simulation results use $v = 0.3125$ sites per kMC cycles, and $S = 0.002175$ per kMC cycles. The blue curve is the simulation (kMC) results, and the red curve is the theoretical prediction ($1/T$, see Eq. (3)). The theory is valid if $1/\alpha - v/S > 0$, and the critical point in this case is $\alpha^* = 0.00456$.

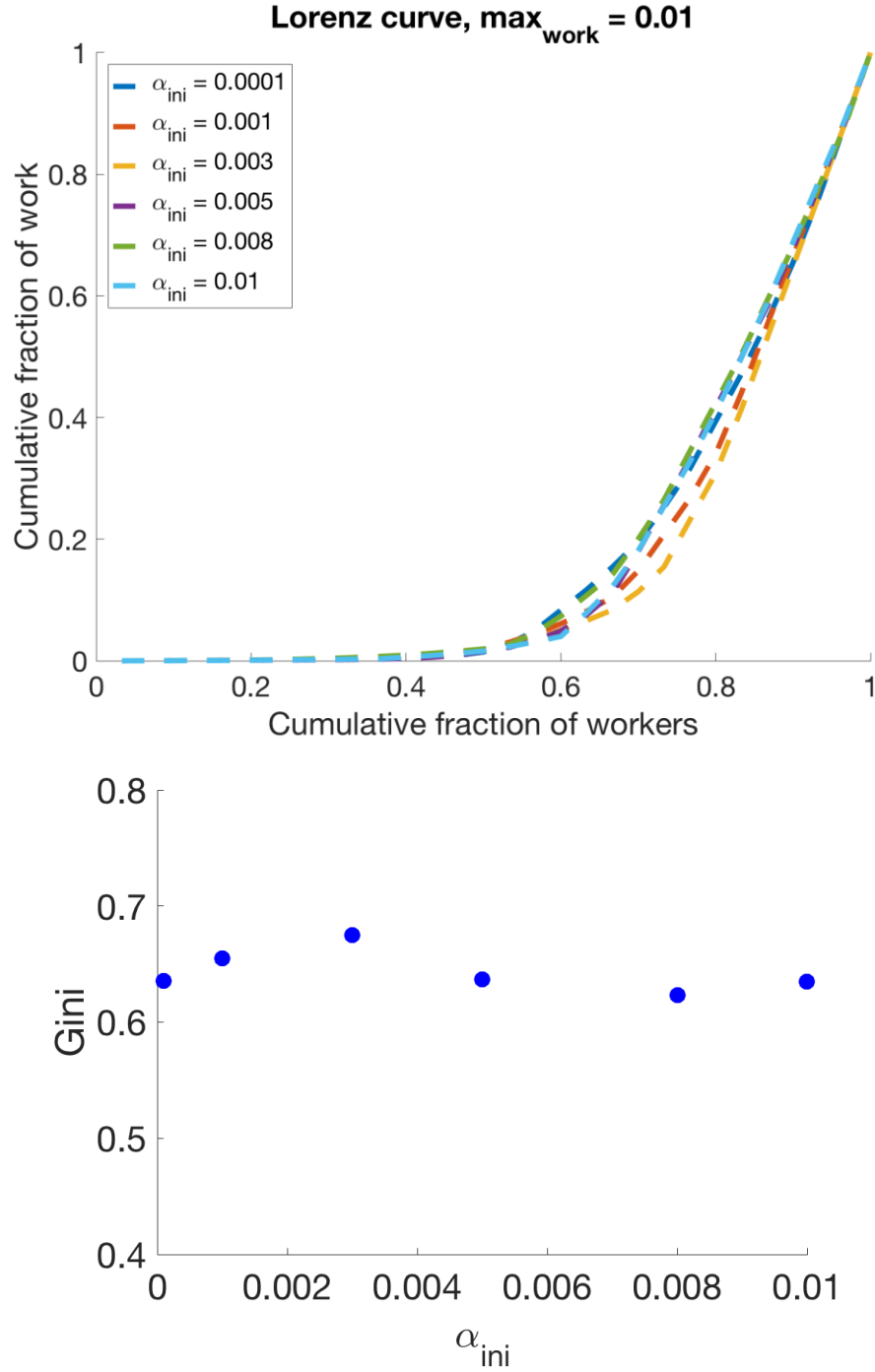


Fig. S16. The Lorenz curves and Gini coefficients that result from training with different values for the population initial workload α_{ini} . The training factor q is $1/0.9$, and the maximum workload is 0.01 (in the same units as α). The total number of ants is 30.

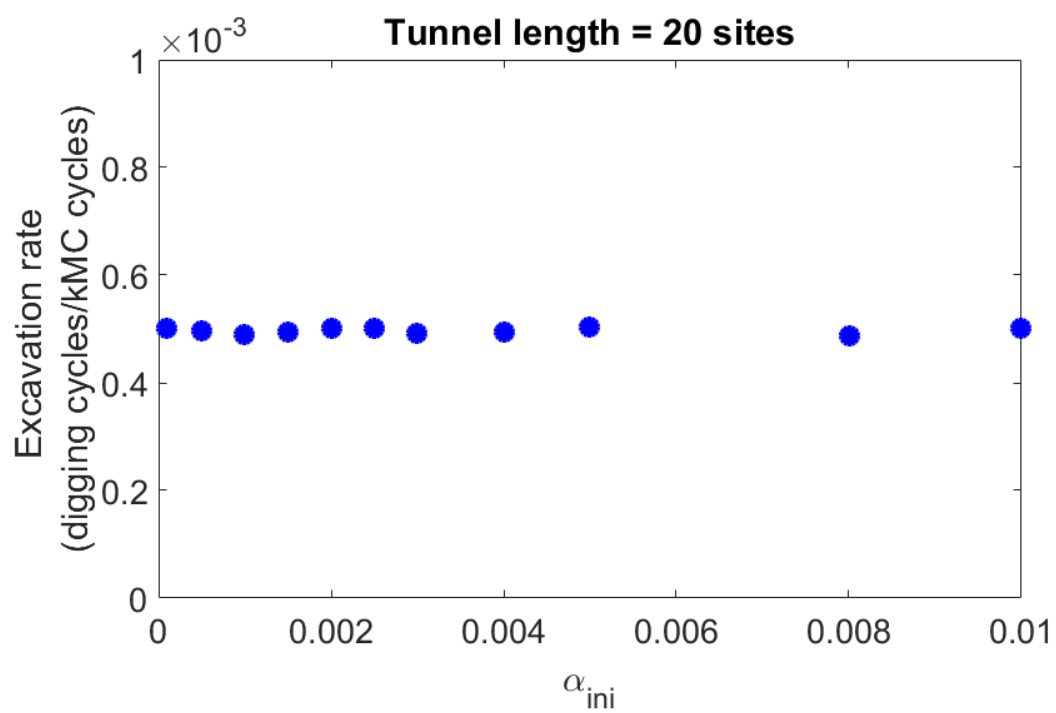


Fig. S17. Excavation rate after training. The final rate is independent of the initial population workload.

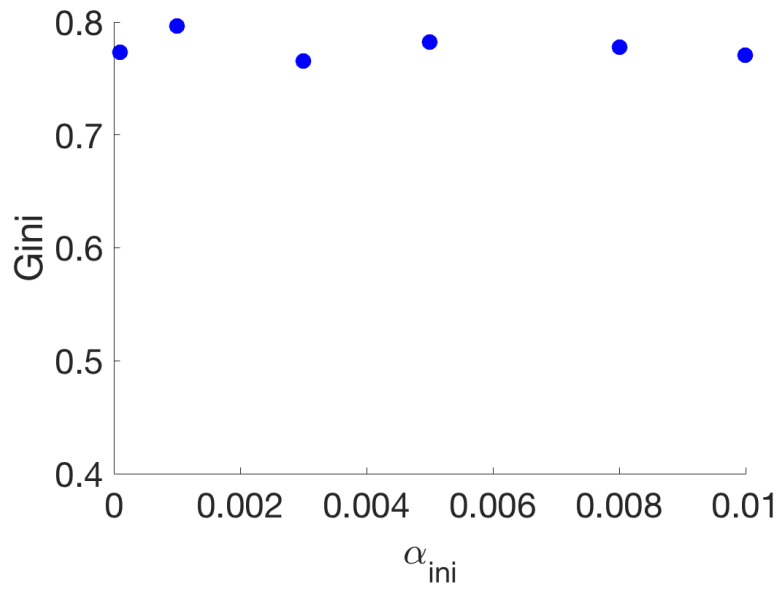


Fig. S18. The Gini coefficients with 60 ants total and $\alpha_{max} = 0.02$. The Gini coefficient is larger than that found in Fig. S18.

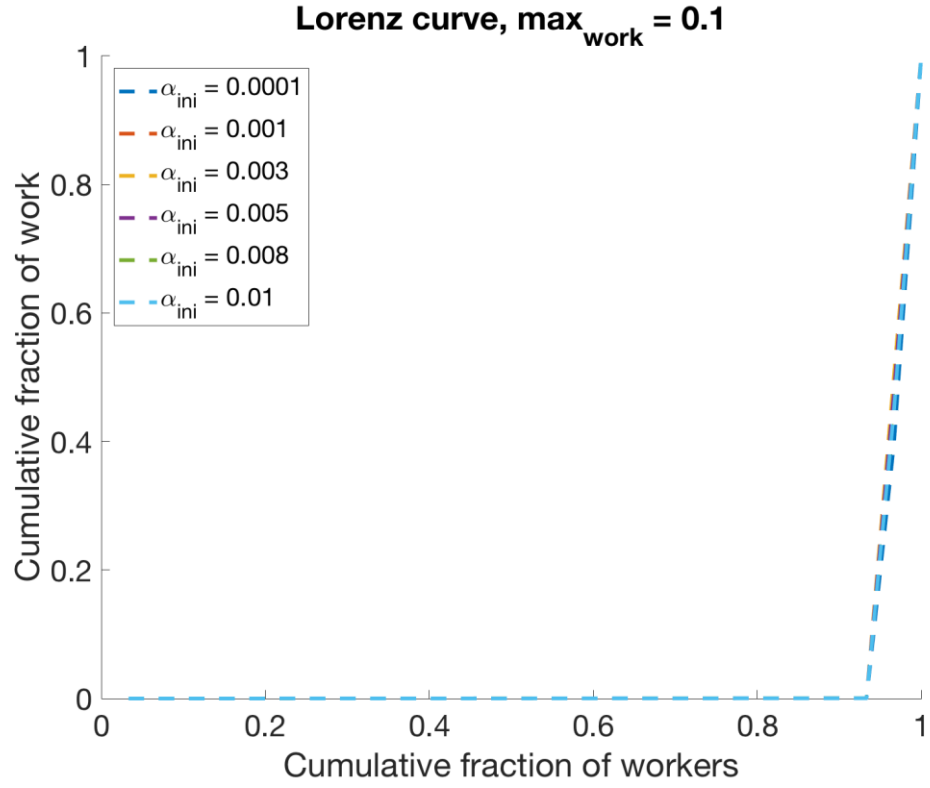


Fig. S19. Lorenz curves with different initial workload α_{ini} . The maximum workload is $\alpha_{\text{max}} = 0.1$, where their Gini coefficients are approximately 0.93.

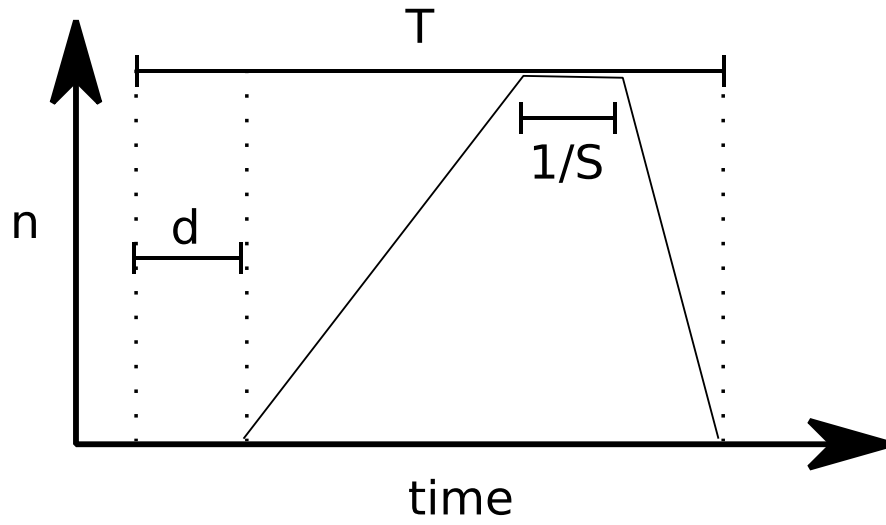


Fig. S20. Schematic of the number of ants versus time in a digging cycle. The y-axis is the overall number of ants in the tunnel, and T is the digging cycle. The delayed time d denotes the time of the first ant enter into the tunnel. The overall number of ants in the digging cycle is the area of the trapezoid, where $1/S$ denotes the time for the last ant to return its direction.

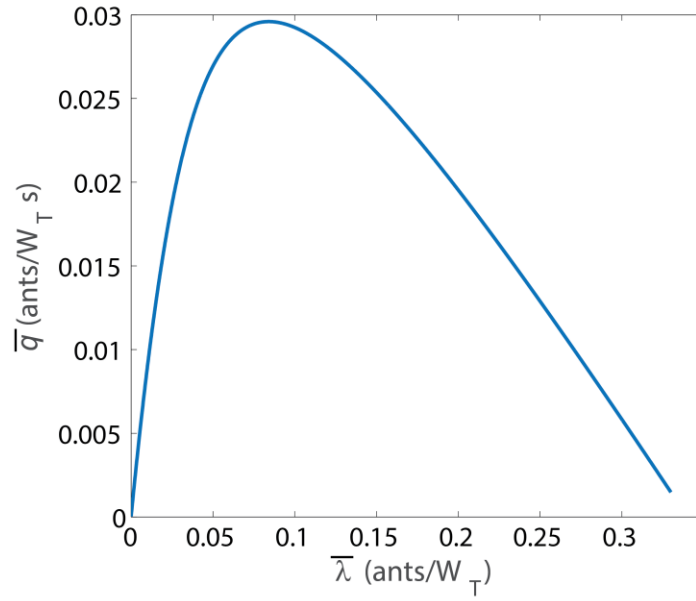


Fig. S21. Fundamental diagram: Flow rate, \bar{q} , vs linear density, $\bar{\lambda}$, where the switching rate at the end of the tunnel (rate of completing excavation) is identical to the rate of reversal when impeded by a retreating excavator.

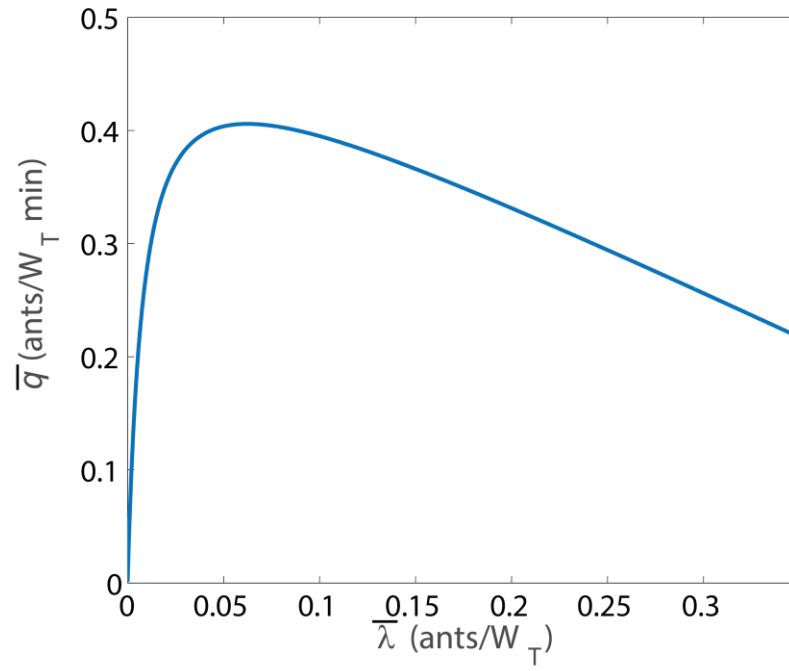


Fig. S22. Fundamental diagram: Flow rate, \bar{q} , vs linear density, $\bar{\lambda}$, with the unique switching rate at the end of the tunnel $g = 0.005v$.

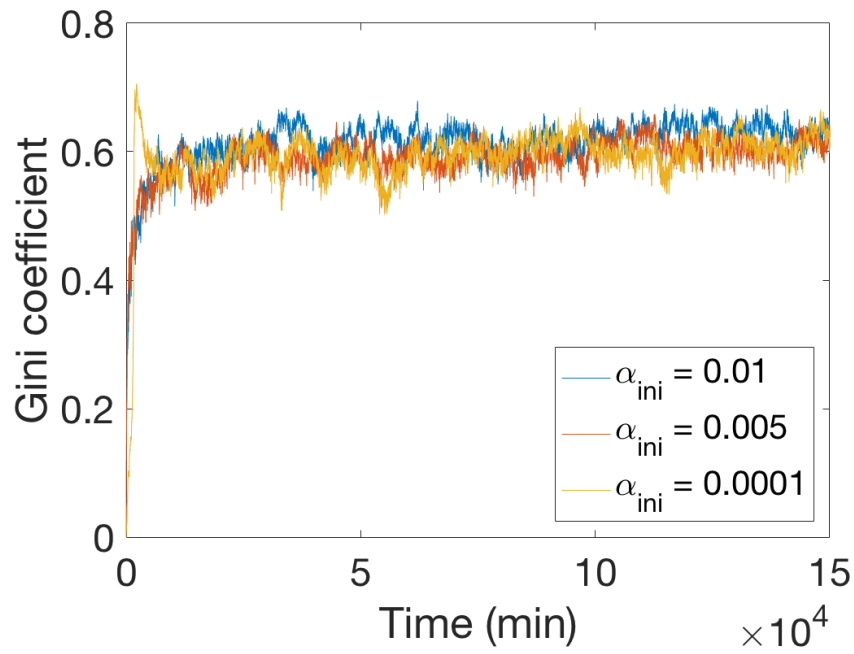


Fig. S23. Gini coefficient vs. time for different initial values of α during kMC simulation of the OAT model in which α changes over time as individual ants increase or decrease their likelihood of reentering the tunnel depending if they reversed before successfully digging.

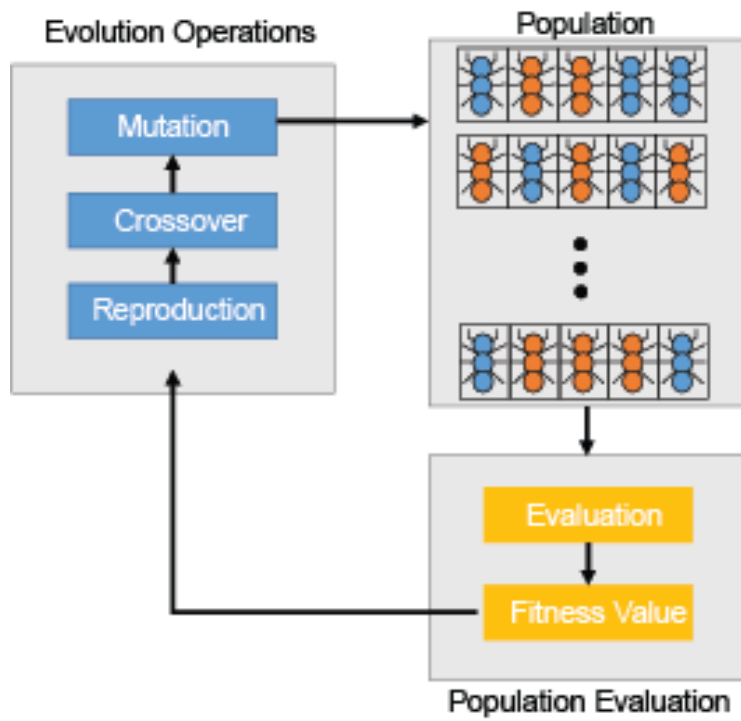


Fig. S24. Diagram illustration of genetic algorithm.

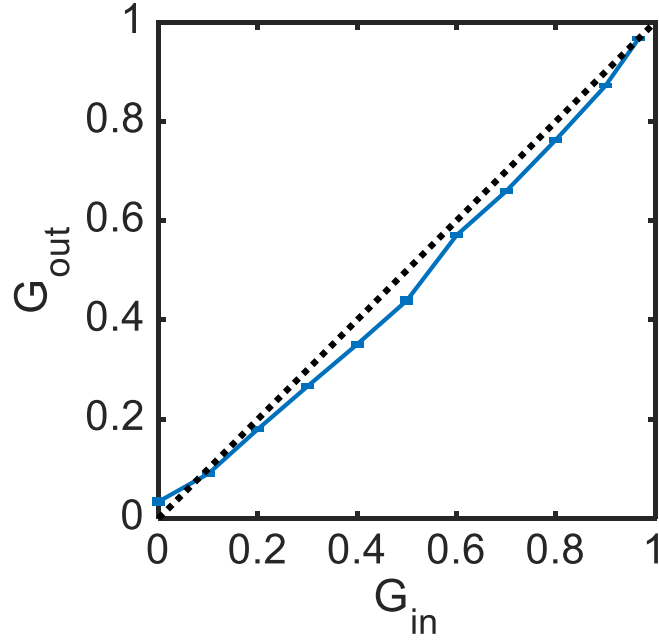


Fig. S25. Measured Gini vs. assigned Gini coefficient for system where initial tunnel length $L=5$ BL, with 30 ants digging for 24 hours. Each point is mean of 5 simulations with error bars shown

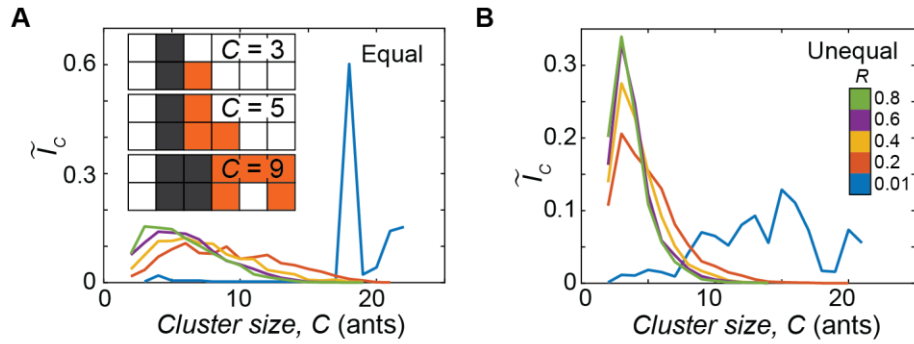


Fig. S26. Proportional number of CA ant clusters, $\tilde{I}_C = I_C/I_{total}$, of different sizes, C , measured over 24 hours for (A) equal and (B) unequal (optimized for 30 CA ants) workload distributions at different reversal probabilities (blue: 0.01, red: 0.2, yellow: 0.4, purple: 0.6, green: 0.8). Sample illustrations for different cluster sizes in (A) inset.

Table S1: Gini coefficients for primary ant digging experiment by epoch

Colony	Moisture	Gini(0-12)	Gini(12-24)	Gini(24-36)	Gini(36-48)	Total 48h
12	10	0.74	0.75	0.76	0.78	0.67
12	1	0.53	0.71	0.77	0.70	0.58
16	10	0.80	0.79	0.80	0.67	0.71
16	1	0.85	0.82	0.83	0.87	0.81
3	10	0.77	0.87	0.90	0.91	0.82
3	1	0.62	0.79	0.70	0.67	0.56

Table S2: Gini Coefficients for ant removal experiments

Colony	Moisture	Removal	Gini
1	10	before	0.85
1	10	after	0.57
2	10	before	0.76
2	10	after	0.69
3	10	before	0.56
3	10	after	0.62

Table S3: Parameters for CA Simulation

Time step, Dt	0.5 s
Ant size	1 cell
Tunnel width (w)	2
Reversal probability (R)	0.34
Sim length	172800 steps (24 hrs)
Time to drop pellet	20 steps
Probability to move sideways (p)	0.52
Probability to move forwards	1
Excavations to grow tunnel size by 1 cell	200
Rest Time	600 steps

Table S4: Robotic ant components

Core components	Purpose
Pixy Camera	Navigation
Magnetometer	Navigation
Gyroscope	Navigation
DC gearmotors	Locomotion
IR Distance Sensors	Obstacle avoidance
Contact Switches	Collision detection
Servo Motors	Environment manipulation
Proximity Sensor	Simulated media feedback
Li-On Battery, Single cell	Power source
Voltage Sensor	Power management

Current Sensor	Power management
Arduino FIO	Data logging
Arduino DUE	Sensor I/O, robot control

Supplemental Movie Captions

Movie S1

Ant activity experiments: Video of an ant (yellow-orange) giving up/reversing when faced with heavy traffic in tunnel.

Movie S2

Ant simulation: Animation of a Cellular Automata (CA) simulation of ants with Active protocol (equal workload distribution) vs. Lorenz protocol (unequal workload). Cell colors denote soil (light grey), tunnel (white). CA ants moving towards the excavation site (orange) and exiting the tunnel (dark grey).

Movie S3

Single robot excavation: Video of a robophysical excavator following a pink line (a guidance trail) and excavating model cohesive granular media; the plastic hollow shells are filled with loose magnets enabling clumps to form.

Movie S4

Collective clogging in robot excavation: Video of robophysical excavators encountering and resolving a clog while excavating model cohesive granular media.

Movie S5

Robophysical experiments comparing excavation protocols: Video comparing Active (top), Reversal (middle) and Lorenz (bottom) protocols implemented on excavating robots. Each Active robot exhibited maximum levels of activity. Reversal robots had a small probability to abandon the excavation attempt if the excavation area could not be reached within pre-defined time interval. Each Lorenz robot was assigned a distinct probability to re-enter tunnel after excavation. The proportion of idle and active robots is similar to observations of ant behavior.

References and Notes

1. A. Okubo, Dynamical aspects of animal grouping: Swarms, schools, flocks, and herds. *Adv. Biophys.* **22**, 1–94 (1986). [doi:10.1016/0065-227X\(86\)90003-1](https://doi.org/10.1016/0065-227X(86)90003-1) [Medline](#)
2. M. Brambilla, E. Ferrante, M. Birattari, M. Dorigo, Swarm robotics: A review from the swarm engineering perspective. *Swarm Intell.* **7**, 1–41 (2013). [doi:10.1007/s11721-012-0075-2](https://doi.org/10.1007/s11721-012-0075-2)
3. M. Marchetti, J. F. Joanny, S. Ramaswamy, T. B. Liverpool, J. Prost, M. Rao, R. A. Simha, Hydrodynamics of soft active matter. *Rev. Mod. Phys.* **85**, 1143–1189 (2013). [doi:10.1103/RevModPhys.85.1143](https://doi.org/10.1103/RevModPhys.85.1143)
4. D. Helbing, Traffic and related self-driven many-particle systems. *Rev. Mod. Phys.* **73**, 1067–1141 (2001). [doi:10.1103/RevModPhys.73.1067](https://doi.org/10.1103/RevModPhys.73.1067)
5. N. C. Darnton, L. Turner, S. Rojevsky, H. C. Berg, Dynamics of bacterial swarming. *Biophys. J.* **98**, 2082–2090 (2010). [doi:10.1016/j.bpj.2010.01.053](https://doi.org/10.1016/j.bpj.2010.01.053) [Medline](#)
6. E. Méhes, T. Vicsek, Collective motion of cells: From experiments to models. *Integr. Biol. (Camb.)* **6**, 831–854 (2014). [doi:10.1039/C4IB00115J](https://doi.org/10.1039/C4IB00115J) [Medline](#)
7. A. Garcimartín, J. M. Pastor, L. M. Ferrer, J. J. Ramos, C. Martín-Gómez, I. Zuriguel, Flow and clogging of a sheep herd passing through a bottleneck. *Phys. Rev. E Stat. Nonlin. Soft Matter Phys.* **91**, 022808 (2015). [doi:10.1103/PhysRevE.91.022808](https://doi.org/10.1103/PhysRevE.91.022808) [Medline](#)
8. L. Giomi, N. Hawley-Weld, L. Mahadevan, Swarming, swirling and stasis in sequestered bristle-bots. *Proc. R. Soc. London A Math. Phys. Sci.* **469**, 20120637 (2013). [doi:10.1098/rspa.2012.0637](https://doi.org/10.1098/rspa.2012.0637)
9. N. Gravish, G. Gold, A. Zangwill, M. A. D. Goodisman, D. I. Goldman, Glass-like dynamics in confined and congested ant traffic. *Soft Matter* **11**, 6552–6561 (2015). [doi:10.1039/C5SM00693G](https://doi.org/10.1039/C5SM00693G) [Medline](#)
10. D. M. Gordon, The organization of work in social insect colonies. *Nature* **380**, 121–124 (1996). [doi:10.1038/380121a0](https://doi.org/10.1038/380121a0)
11. D. Cassill, W. R. Tschinkel, S. B. Vinson, Nest complexity, group size and brood rearing in the fire ant, *Solenopsis invicta*. *Insectes Soc.* **49**, 158–163 (2002). [doi:10.1007/s00040-002-8296-9](https://doi.org/10.1007/s00040-002-8296-9)
12. N. Gravish, D. Monaenkova, M. A. Goodisman, D. I. Goldman, Climbing, falling, and jamming during ant locomotion in confined environments. *Proc. Natl. Acad. Sci. U.S.A.* **110**, 9746–9751 (2013). [doi:10.1073/pnas.1302428110](https://doi.org/10.1073/pnas.1302428110) [Medline](#)
13. D. Monaenkova, N. Gravish, G. Rodriguez, R. Kutner, M. A. D. Goodisman, D. I. Goldman, Behavioral and mechanical determinants of collective subsurface nest excavation. *J. Exp. Biol.* **218**, 1295–1305 (2015). [doi:10.1242/jeb.113795](https://doi.org/10.1242/jeb.113795) [Medline](#)
14. V. Linevich, D. Monaenkova, D. I. Goldman, Robophysical study of excavation in confined environments. *Artif. Life Robot.* **21**, 460–465 (2016). [doi:10.1007/s10015-016-0317-2](https://doi.org/10.1007/s10015-016-0317-2)
15. P. Tenczar, C. C. Lutz, V. D. Rao, N. Goldenfeld, G. E. Robinson, Automated monitoring reveals extreme interindividual variation and plasticity in honeybee foraging activity levels. *Anim. Behav.* **95**, 41–48 (2014). [doi:10.1016/j.anbehav.2014.06.006](https://doi.org/10.1016/j.anbehav.2014.06.006)

16. E. J. Robinson, O. Feinerman, N. R. Franks, Flexible task allocation and the organization of work in ants. *Proc. Biol. Sci.* **276**, 4373–4380 (2009). [doi:10.1098/rspb.2009.1244](https://doi.org/10.1098/rspb.2009.1244) [Medline](#)
17. D. M. Gordon, The evolution of the algorithms for collective behavior. *Cell Syst.* **3**, 514–520 (2016). [doi:10.1016/j.cels.2016.10.013](https://doi.org/10.1016/j.cels.2016.10.013) [Medline](#)
18. V. Fourcassié, A. Dussutour, J. L. Deneubourg, Ant traffic rules. *J. Exp. Biol.* **213**, 2357–2363 (2010). [doi:10.1242/jeb.031237](https://doi.org/10.1242/jeb.031237) [Medline](#)
19. A. John, A. Schadschneider, D. Chowdhury, K. Nishinari, Collective effects in traffic on bi-directional ant trails. *J. Theor. Biol.* **231**, 279–285 (2004). [doi:10.1016/j.jtbi.2004.06.022](https://doi.org/10.1016/j.jtbi.2004.06.022) [Medline](#)
20. N. Gravish, M. Garcia, N. Mazouchova, L. Levy, P. B. Umbanhowar, M. A. D. Goodisman, D. I. Goldman, Effects of worker size on the dynamics of fire ant tunnel construction. *J. R. Soc. Interface* **9**, 3312–3322 (2012). [doi:10.1098/rsif.2012.0423](https://doi.org/10.1098/rsif.2012.0423) [Medline](#)
21. C. R. Reid, M. J. Lutz, S. Powell, A. B. Kao, I. D. Couzin, S. Garnier, Army ants dynamically adjust living bridges in response to a cost-benefit trade-off. *Proc. Natl. Acad. Sci. U.S.A.* **112**, 15113–15118 (2015). [doi:10.1073/pnas.1512241112](https://doi.org/10.1073/pnas.1512241112) [Medline](#)
22. C. Gershenson, D. Helbing, When slower is faster. *Complexity* **21**, 9–15 (2015). [doi:10.1002/cplx.21736](https://doi.org/10.1002/cplx.21736)
23. K. Nagel, M. Schreckenberg, A cellular automaton model for freeway traffic. *J. Phys. I* **2**, 2221–2229 (1992). [doi:10.1051/jp1:1992277](https://doi.org/10.1051/jp1:1992277)
24. R. Kühne, “Traffic patterns in unstable traffic flow on freeways,” in *Highway Capacity and Level of Service: Proceedings of the International Symposium on Highway Capacity, Karlsruhe, 24–27 July 1991*, U. Brannolte, Ed. (CRC Press, 1991).
25. H.-S. Kuan, M. D. Betterton, Phase-plane analysis of the totally asymmetric simple exclusion process with binding kinetics and switching between antiparallel lanes. *Phys. Rev. E* **94**, 022419 (2016). [doi:10.1103/PhysRevE.94.022419](https://doi.org/10.1103/PhysRevE.94.022419) [Medline](#)
26. J. Aguilar, T. Zhang, F. Qian, M. Kingsbury, B. McInroe, N. Mazouchova, C. Li, R. Maladen, C. Gong, M. Travers, R. L. Hatton, H. Choset, P. B. Umbanhowar, D. I. Goldman, A review on locomotion robophysics: The study of movement at the intersection of robotics, soft matter and dynamical systems. *Rep. Prog. Phys.* **79**, 110001 (2016). [doi:10.1088/0034-4885/79/11/110001](https://doi.org/10.1088/0034-4885/79/11/110001) [Medline](#)
27. M. J. Mataric, “Designing emergent behaviors: From local interactions to collective intelligence,” in *From Animals to Animats 2: Proceedings of the Second International Conference on Simulation of Adaptive Behavior*, J.-A. Meyer, H. L. Roitblat, S. W. Wilson, Eds. (MIT Press, 1993), pp. 432–441.
28. U. Borrmann, L. Wang, A. D. Ames, M. Egerstedt, Control barrier certificates for safe swarm behavior. *IFAC-PapersOnLine* **48**, 68–73 (2015). [doi:10.1016/j.ifacol.2015.11.154](https://doi.org/10.1016/j.ifacol.2015.11.154)
29. G. S. Redner, M. F. Hagan, A. Baskaran, Structure and dynamics of a phase-separating active colloidal fluid. *Phys. Rev. Lett.* **110**, 055701 (2013). [doi:10.1103/PhysRevLett.110.055701](https://doi.org/10.1103/PhysRevLett.110.055701) [Medline](#)

30. D. I. Goldman, H. L. Swinney, Signatures of glass formation in a fluidized bed of hard spheres. *Phys. Rev. Lett.* **96**, 145702 (2006). [doi:10.1103/PhysRevLett.96.145702](https://doi.org/10.1103/PhysRevLett.96.145702) [Medline](#)
31. H.-S. Kuan, R. Blackwell, L. E. Hough, M. A. Glaser, M. D. Betterton, Hysteresis, reentrance, and glassy dynamics in systems of self-propelled rods. *Phys. Rev. E Stat. Nonlin. Soft Matter Phys.* **92**, 060501 (2015). [doi:10.1103/PhysRevE.92.060501](https://doi.org/10.1103/PhysRevE.92.060501) [Medline](#)
32. K. Jayaram, R. J. Full, Cockroaches traverse crevices, crawl rapidly in confined spaces, and inspire a soft, legged robot. *Proc. Natl. Acad. Sci. U.S.A.* **113**, E950–E957 (2016). [doi:10.1073/pnas.1514591113](https://doi.org/10.1073/pnas.1514591113) [Medline](#)
33. S. Li, Q. Jiang, S. Liu, Y. Zhang, Y. Tian, C. Song, J. Wang, Y. Zou, G. J. Anderson, J.-Y. Han, Y. Chang, Y. Liu, C. Zhang, L. Chen, G. Zhou, G. Nie, H. Yan, B. Ding, Y. Zhao, A DNA nanorobot functions as a cancer therapeutic in response to a molecular trigger in vivo. *Nat. Biotechnol.* **36**, 258–264 (2018). [doi:10.1038/nbt.4071](https://doi.org/10.1038/nbt.4071) [Medline](#)
34. W. Liu, A. F. Winfield, J. Sa, J. Chen, L. Dou, Towards energy optimization: Emergent task allocation in a swarm of foraging robots. *Adapt. Behav.* **15**, 289–305 (2007). [doi:10.1177/1059712307082088](https://doi.org/10.1177/1059712307082088)
35. D. Jouvenaz, G. Allen, W. Banks, D. P. Wojcik, A survey for pathogens of fire ants, *Solenopsis* spp., in the southeastern United States. *Fla. Entomol.* **60**, 275–279 (1977). [doi:10.2307/3493922](https://doi.org/10.2307/3493922)
36. MathWorks, Global Optimization Toolbox (R2016a) (2016).
37. V. Linevich, Master's thesis, Georgia Institute of Technology, (2015).
38. M. J. Krieger, J.-B. Billeter, The call of duty: Self-organised task allocation in a population of up to twelve mobile robots. *Robot. Auton. Syst.* **30**, 65–84 (2000). [doi:10.1016/S0921-8890\(99\)00065-2](https://doi.org/10.1016/S0921-8890(99)00065-2)
39. S. Yun, M. Schwager, D. Rus, in *Robotics Research*, C. Pradalier, R. Siegwart, G. Hirzinger, Eds. (Springer Tracts in Advanced Robotics, vol. 70, Springer, 2011), pp. 607–623.
40. K. N. Nordstrom, J. P. Gollub, D. J. Durian, Dynamical heterogeneity in soft-particle suspensions under shear. *Phys. Rev. E Stat. Nonlin. Soft Matter Phys.* **84**, 021403 (2011). [doi:10.1103/PhysRevE.84.021403](https://doi.org/10.1103/PhysRevE.84.021403) [Medline](#)
41. Z. Jiang, Q. Kemao, H. Miao, J. Yang, L. Tang, Path-independent digital image correlation with high accuracy, speed and robustness. *Opt. Lasers Eng.* **65**, 93–102 (2015). [doi:10.1016/j.optlaseng.2014.06.011](https://doi.org/10.1016/j.optlaseng.2014.06.011)